TOWARD A LABEL-FREE SINGLE MOLECULE, FUNCTIONALIZED, SIZE/MASS SPECTROMETER FOR BIO-COMPLEX ANALYSIS WITH MICROCAVITIES

THESIS

Submitted in Partial Fulfillment of

the Requirements for

the Degree of

MASTER OF SCIENCE (Chemical Engineering)

at the

NEW YORK UNIVERSITY
POLYTECHNIC SCHOOL OF ENGINEERING

by

Eshan Treasurer

September 2015

TOWARD A LABEL-FREE SINGLE MOLECULE, FUNCTIONALIZED, SIZE/MASS SPECTROMETER FOR BIO-COMPLEX ANALYSIS WITH MICROCAVITIES

THESIS

Submitted in Partial Fulfillment of

the Requirements for

the Degree of

MASTER OF SCIENCE (Chemical Engineering)

at the

NEW YORK UNIVERSITY
POLYTECHNIC SCHOOL OF ENGINEERING

by

Eshan Treasurer

September 2015

Approved:

_____
Adviser Signature

_____
Date

_____
Department Head Signature

_____
Date

Copy No. # ____1____
University # _N13600226_

Approved by the Guidance Committee

Major: Chemical Engineering

Dr. Rastislav Levicky
Donald F Othmer Associate Professor of Chemical and Biomolecular Engineering

_____
Date

Dr. Stephen Arnold
Thomas Potts University Professor of Physics

_____
Date

Dr. Jin R Kim
Associate Professor of Chemical and Biomolecular Engineering

_____
Date

VITA

Eshan Treasurer was born on February 20, 1991 in Ann Arbor, Michigan. Formal education was done in the public school system of Stamford, Connecticut. In September 2009, he began studying at NYU Polytechnic School of Engineering for a combined BS/MS in Chemical Engineering. Research presented in this thesis started on January, 2015 and will continue into a Ph.D. program.

Acknowledgements

I want to express my gratitude to my advisor, Dr. Rastislav Levicky, for giving me a chance to find my way through this Master's program; always guiding me patiently and insightfully. Thank you for your continual effort.

I want to thank my co-advisor, Dr. Stephen Arnold, for spending countless hours mentoring and teaching me. Your hard work and inventive style have inspired me with a great interest for physics and optics.

I'm indebted to Dr. David Keng. You've sacrificed so many weekends to teach me the ropes and have been the go-to-guy any time that I needed it. I can't thank you enough for that.

Mike Rath, thanks for making the best tapered fibers on the East coast and in general for being a great lab mate. I'd also like to thank Dr. Jin Ryoun Kim for being on my defense committee and I wanted to thank all of my fellow students within Dr. Levicky's and Dr. Kim's labs' that have made the journey so much fun. Ursula Koniges, thank you for being an amazing cubicle mate. Howard Chiang, Sade Ruffin, Elvin Feng, Vladislav Frenkel, Edward Chau, Jason Candreva, Vandan Shah, and to many others, thank you for being an absolutely awesome bunch of human beings.

Our administrators, Carmen Villafane and Magda Guadalupe, have also been diligently looking out for all of us; thanks for being such kind, caring people.

Lastly, I wanted to thank my parents, Yash and Urvee Treasurer, for their support and love throughout this program. I'm ever grateful for having you both as parents.

I look forward to working with all of you in the coming years throughout my Ph.D.

Dedicated to

the loving memory of

Dr. (Mrs.) Purvi Desai-Haribhakti

We'll miss you.

ABSTRACT

TOWARD A LABEL-FREE SINGLE MOLECULE, FUNCTIONALIZED, SIZE/MASS SPECTROMETER FOR BIO-COMPLEX ANALYSIS WITH MICROCAVITIES

by

Eshan Treasurer

Advisor: Prof. Rastislav Levicky
Co-Advisor: Prof. Stephen Arnold

Submitted in Partial Fulfillment of the Requirements for

the Degree of Master of Science (Chemical Engineering)

September 2015

Biomolecular complexes are some of the most intricate molecular arrangements that lend themselves to a myriad of life supporting roles. They can also be very challenging systems to characterize. The aim of this thesis is to develop a new tool for analysis of biomolecular complexes at the single molecule level in a label-free fashion with Whispering Gallery Mode (WGM) technology as a platform. The goal of this project seeks to push the limits of the WGM sensor sensitivity beyond Abbe's diffraction limits in order to resolve the cohort of proteins involved within an RNA polymerase (RNAP) system. Two approaches to toward this goal were considered: (1) a WGM-nanoplasmonic (WGM-NP) hybrid construct and (2) the reduction of the WGM resonator size facilitated by the use of new materials, namely barium titanate (BT) in this thesis. WGM-NP structures have already proven sensitivity limits that are able to resolve individual proteins but have a limited reactive (sensing) volume so that use of more than one plasmonic particle, precisely arranged upon the WGM resonator surface, may be necessary to facilitate RNAP sensing.

The Light Force Assembly method, introduced as a new feature to WGM spheroidal resonators within this thesis, is shown to provide first steps toward such a fabrication capability. Along the second direction, BT WGM spheroidal resonators with diameter of 20 μm have been experimentally shown in this thesis to provide much greater sensitivity than silica resonators while being able to confine light very efficiently ($Q \approx 1E6$). It was also theoretically shown that yet smaller radii resonators would be necessary to sense proteins within an RNAP complex, however, the high Q values achieved show that further size reduction should be possible.

Table of Contents

List of Figures

List of Abbreviations

RNA = Ribonucleic Acid

RNAP = Ribonucleic Acid Polymerase

DNA = Deoxyribonucleic Acid

EM = Electromagnetic

nm = nanometer

μm = micrometer

WGM = whispering gallery mode

BT = Barium Titanate ($BaTiO_3$)

LSPR = localized surface plasmon resonance

LFA = light force assembly

Å = Angstrom

pm = picometer

RSP = reactive sensing principle

TE = transverse electric

TM = transverse magnetic

PD = photodetector

DI = de-ionized

DFB = distributed feed-back

FSR = free spectral range

mW = milli Watts

μW = micro Watts

PDMS = polydimethylsiloxane

L-I curve = Light-Current curve

WGM-NP = Whispering Gallery Mode – Nanoplasmonic

I. DEVELOPING A TOOL FOR BIO-MACROMOLECULAR COMPLEX SENSING

The aims of this project strive toward the eventual development of a size/mass spectrometer that is able to precisely probe the dynamics of a single, label-free, RNA polymerase holoenzyme complex acting upon a DNA template in real-time. The idea is to adapt the unique sensing capabilities of Whispering Gallery Mode (WGM) resonators in order to meet the various challenges involved in detecting interactions within a bio-macromolecular complex. In order to fully characterize such a system the spectrometer must be able to (1) detect individual biomolecules within the range of 50-500kDa, (2) identify individual biomolecules through size determination, (3) sense over a volume sufficiently large enough to allow tracking of movement of RNA polymerase (RNAP) over tens of nanometers, (4) ascertain degree of co-localization of biomolecules and (5) measure in real-time without the use of any kind of modification to the biomolecules. While the time scale over which all five components of the sensor can be designed and integrated into a WGM system is arguably longer than what was available over the duration of this master's study it was the goal to be able to explore how viable it would be to meet such requirements and to start on the development of such a size/mass spectrometer.

A. BIO-COMPLEX DETECTION & ANALYSIS

Bio-complex and bio-complex functions are defined within spatial, structural (chemically), and temporal dimensions. This degree of complexity affords them a myriad of possible operations with which to participate in varied and essential life sustaining functions but are the reason they are difficult to characterize.

It is yet only generally known how polymerase systems work from protein interaction principles and kinetic simulations.[1] Experimentally, precise characterization of bio-complex mechanics has been primarily plagued by the inability to receive signal from only a single bio-complex unit. As an example, a 2011 study by Weisshaar *et al.*[2] measures the spatial distribution and diffusive motion of RNAP in live E. coli cells using fluorescence microscopy and measures the mean apparent diffusion constant, 0.22 ± 0.16 $\mu m^2 s^{-1}$, within a 70% uncertainty. Unfortunately signal from an ensemble of complexes can lead to the averaging out of fine temporal and spatial resolution necessary to understanding underlying dynamics of the system.[3,4,5,6] The most important of the five fulfillments of this spectrometer is the ability to sense down to a size where the organization and function of a single bio-complex can be addressed, thus avoiding the limits of averaging inherent in ensemble techniques.

The dynamics within a bio-complex involve a cohort of cofactor proteins which regulate the binding of apoenzymes and are involved in assembly and disassembly processes that occur in an *ad-hoc* stepwise fashion.[7] Understanding the mode of binding would involve, not only, the ability to detect these co-factor proteins but also the ability to distinguish one from another; another capability WGM sensors are demonstrably suited for through size determination.[8] It is known to be the case that this assembly serves as a way to allow selective RNAP apoenzyme binding to target promoter regions. [9]

A fully assembled holoenzyme (cofactor proteins + apoenzyme) is generally apt for an incredible variety of functions. In the case of RNAP systems, polymerase must carry out its role over the length of its DNA strand. There are competing models theorizing RNAP's mechanism of movement [10] but it is clear that a few important parameters include

how much time it spends at one location and its ability to 'back-track' is thought to be connected to diverse roles within the context of genetic regulation, i.e. transcription fidelity, elongation rate control, and other functions.[11] The length of a DNA track which it motors along can be on the order of nanometers a second (~20nucleotides/second[12]) and therefore it is important to construct a sensing scheme that can resolve fine spatial detail over a large track. It should also be noted that it is very important to be able to track a single molecule over this range without incorporating signal from other 'background' events; a functionality that needs additional design considerations.

It may be clear to the reader, by now, of the many layers and pieces that comprise the typical definition of a "bio-complex" and, why then, little progress has been made characterizing such systems thus far. The justification for being able to study such structures is also by now, perhaps, satisfying. The latter two considerations that have been discussed (that is being able to track polymerase over a large enough volume and being able to separate its signal out from those of other events in the background) were not pursued over the course of this thesis. However, that of being able to sense finely enough and that of being able to differentiate molecules were indeed shown to be possible.

It is also of interest to briefly discuss why whispering gallery mode sensors form an ideal candidate for this bioanalytical need by comparing them with the capabilities of other measurement techniques.

B. CURRENT DETECTION TECHNIQUES

One of the most attractive features of a whispering gallery mode sensor is the ability to sense molecules without the use of a fluorescent tag. Most existing single-molecule

techniques involve fluorescence-based labeling methods in conjunction with Förster resonance energy transfer[13], total internal reflection fluorescence microscopy[14], zero-mode waveguide[15], or fluorescence recovery after photo-bleaching[16] approaches. In order to observe small proteins fluorescing the technique must be able to 'see' past the far-field diffraction limit and while super microscopy techniques are able to see below this limit [17] there are other potential challenges with using labels. It is possible to imagine that the presence of a fluorescent tag may influence molecular interactions under investigation in unexpected ways. In a technical sense, concerns of fluorescent bleaching may hamper the time-scale of observations. Notwithstanding other potential challenges, there may also not be enough fluorescent tags with sufficiently differentiated emission spectra to simultaneously track all molecules of interest in an experiment.

There are, of course, existing label-free assays. Most notably the use of nanoplasmonics have given rise to much more sensitive measurement by way of tracking shifts in plasmon resonance[18,19,20]. Nanoplasmonic structures have even been used in conjunction with whispering gallery mode resonators[21] with great effect; this arrangement was able to push the limits of noise-bound sensitivity down to about 5 kDa. However, bio-macromolecular complex analysis has an additional requirement of ensuring that measured signals refer to events occurring within the same bio-complex. While fluorescence microscopy methods have provided the necessary spatial resolution to achieve this, most label free methods have not provided exactly analogous comparability but do feature configurations that allow for it (e.g. plasmonic hot-spots).

A second limitation arises from the nature of electromagnetic (EM) fields produced by plasmonic surfaces, which are uneven and typically range on the order of several

nanometers, which could put restraints on the size of the analyte of interest. A small sensing volume also inhibits use of additional components or linkers that may be needed to isolate a bio-complex from interference of the solid support it rests on. As a result, sensor design becomes more complicated in order to overcome such problems.

WGM resonators already have many of the basic functionalities required of such a sensor which can be extended as needed through appropriate modifications. In particular, WGM sensing is label-free, has demonstrated single-molecule detection, has the ability to locate and size particles, [22] and also has the additional feature of being able to trap particles with nanometer precision on its surface.

C. APPROACH

Two key challenges to creating a fully functional bio-complex sensor were considered in this thesis. Firstly, increasing the sensitivity of the bare microcavity resonator and secondly, facilitating a precise arrangement of nanoshells on the microcavity surface that would allow for bio-complex sensing.

There a few ways that one can take in order to increase sensitivity of bare cavity WGM sensing. This thesis considered decreasing the size of the resonator cavity and increasing its refractive index, as compared to typical 80 μm diameter silica resonator cavities. In particular, ~ 20μm diameter barium titanate glass ($BaTiO_3$; BT) microspheroids were tested as suitable cavity materials. High refractive index glasses have thus far been little explored as a tool for bioanalytics within the context of whispering gallery mode resonators. However, in theory use of smaller, higher refractive index cavities allows

greater sensitivity to perturbations as compared to larger, lower refractive index cavities. Moreover, accurate analytical expressions for predicting the expected signal due to an analyte can be used.

It is also important to note that prior work has already demonstrated use of gold nanoshells on top of bare WGM cavities to detect single proteins. Therefore an effort to adapt nanoplasmonic technology has also been initiated. In this case, since adequate sensitivity has already been demonstrated, the challenge is to address how to best realize accurate bio-complex analytics. Light Force Assembly (LFA) will be introduced as a new feature to the whispering gallery mode sensor in this thesis; it could serve as a way to help arrange nanoshells on the resonator surface in a way that could enhance bio-complex analysis.

II. RELEVANT THEORY

A. INTRODUCTION TO WGM PHENOMENA

The concept of whispering gallery mode resonance is owed to Lord Rayleigh who first noticed the unique acoustic phenomenon within St Paul's Cathedral circa 1878.

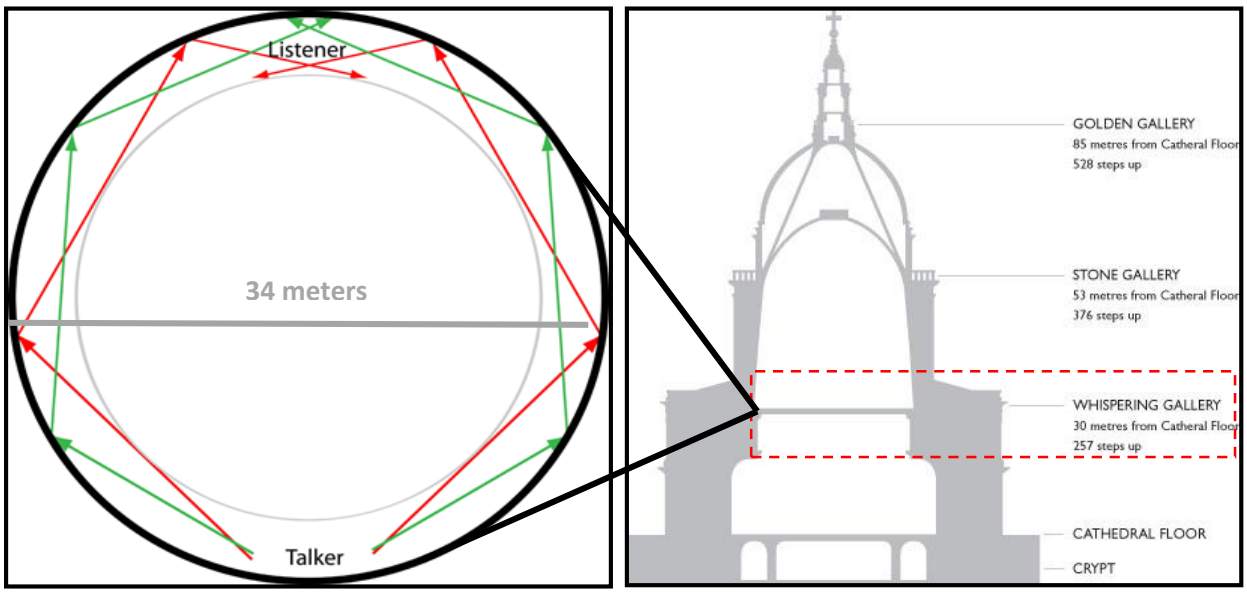

Figure 1: Cross section of St. Paul's Cathedral Whispering Gallery. Ray-trace depiction of polychromatic sound waves propagating circumferentially.

Right: credit to www.stpauls.co.uk [23]

Imagine two people standing opposite each other within a circular enclosure, both adjacent the walls (as in *Fig.* 1). A whisper from one can be carried a remarkable 34 meters away[24] by the walls of St Paul's dome. Empirically speaking, we may understand the relative rarity of whispering gallery waves as a sign that it require very specific conditions in order to occur. Indeed what Rayleigh had uncovered was the proper geometry to support this curvilinear propagation of sound; so-called acoustic "whispering gallery" waves, it

seemed, to clung to the walls of a concave surface and propagate along its tangents without the significant loss of intensity.[25]

It turns out that electromagnetic waves can be confined to circumferential paths, or modes, with similar geometry, however as one could expect, the precise morphology (size, shape, material) of the cavity would have to be different. Indeed, optical whispering gallery modes have been well studied and are demonstrably shown to occur inside of amorphous, dielectric microcavities. It is easy enough to picture photons entering a high refractive index cavity and bouncing off the boundaries before leaking out again but what if a ray of light entered the cavity with a close-to-tangent angle? Such a grazing angle of incidence is, within the correct morphology, reflected many times along the periphery of the cavity before leaking out again by maintaining approach angles almost near the required critical angle of total internal reflection at every point along the boundary (simplified ray-trace representation in *Fig. 2*). As a result, the continual propagation of light may be supported by trapping light temporally within certain orbits along the interior microcavity surface.

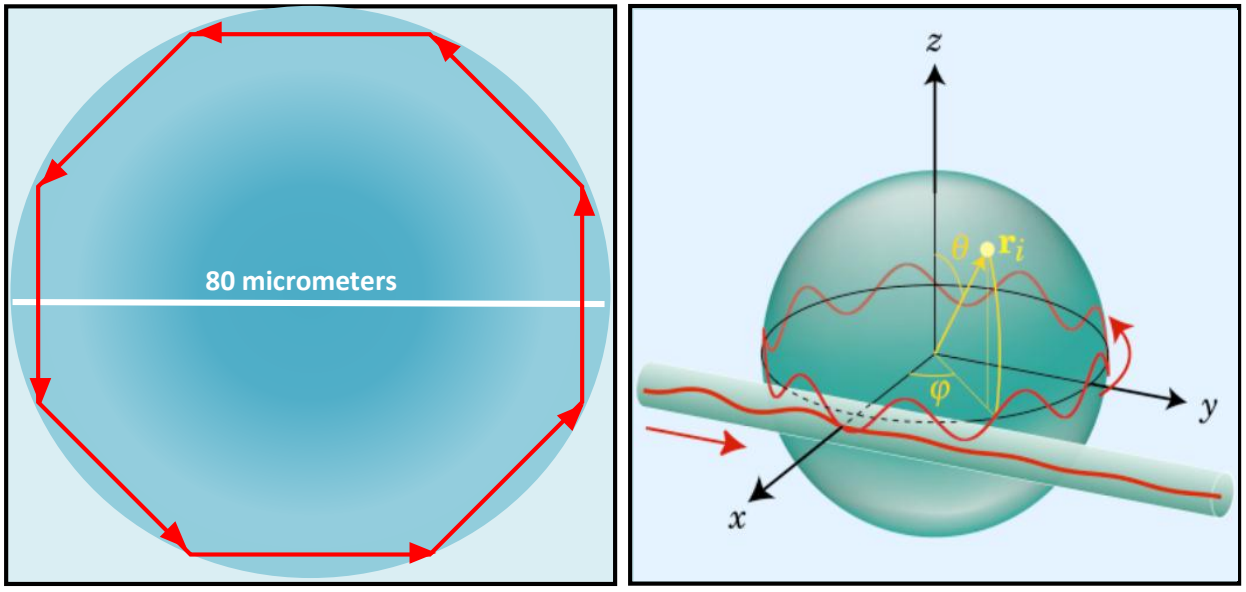

Figure 2 ***Left:*** **Ray-trace of photon orbit due to total internal reflection** ***Right:*** **Wave depiction of light coupled in through a fiber optic cable. Dubbed 'Photonic Atom'.**[26]

These optical modes can be described by solving the Helmholtz equation for homogenous spheres in spherical coordinates. [27] However, more intuitive solutions can be derived by re-arranging Maxwell's equations for Mie spheres to look like Schrödinger's equation and translating well-understood solutions to the Bohr atom to the WGM system.[28] This analogy has been dubbed the 'Photonic Atom' and likens the orbit of light to the orbit of an electron around the nucleus of a hydrogen atom. [29] Without going into the derivation of such a system it is important to highlight what the implications of such a model are. An immediate utility of the atomic analog is illustrated by modeling a photon within the microsphere as being trapped by an effective potential well.

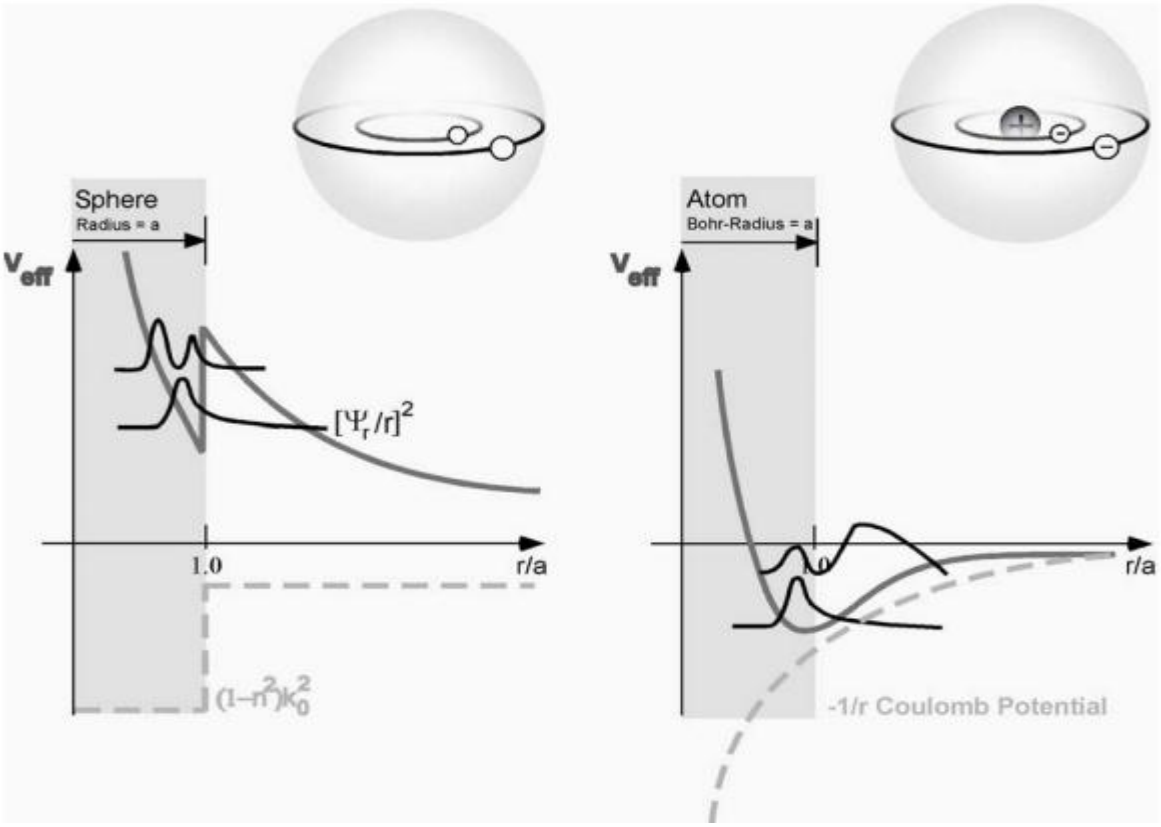

Figure 3: A sketch depicting the analogy between the 'photonic atom' (left) and a Bohr atom (right). In the photonic atom the wave functions describing the photons are trapped in an effective potential well created at the refractive index boundary interface of sphere and surrounding medium. [30]

In order to escape a photon must be able to tunnel through the potential well, which can be physically represented through a small caustic region near the sphere surface (defined by the potential offset which coincides with the dashed potential lines). The solutions to ψ^2 show intensity peaks at particular wave lengths (nestled inside of k_0) within a certain refractive index environment as is seen in Fig. 3 and can be stimulated by external fields to resonate. These resonant structures and their modalities are the central concepts that all study of WGM phenomena revolve around.

Another major outcome arises by assigning the photon in circulation a quantized angular momentum. At the equator of the sphere, the optical path of light divided by its wavelength must satisfy:

$$\frac{2\pi R n_{eff}}{\lambda_0} = m \qquad \textbf{Eq. 1}$$

Where R is radius, n_{eff} is effective refractive index, λ_0 is wavelength in vacuum, *m* is the azimuthal angular momentum quantum number. Another consequence of this is realizing that, just as in the Bohr atom, stable resonances only occur when the light is able to circumnavigate the cavity and return in phase with its starting point; in other words, when *m* is an integer number.

Eq.1 has important experimental consequences. For example, if we change the radius of the resonator, R, and keep the azimuthal angular momentum number, *m*, the same, then it is readily apparent how the wavelength requirement of the light inside changes:

$$\frac{\partial \lambda}{\lambda} = \frac{\partial R}{R} \qquad \textbf{Eq. 2}$$

With the same logic applicable to refractive index changes. Eq. 1 is able to give additional insights.

B. INCREASING SENSITIVITY

It is a natural next question to ask *how* a change in size, refractive index or other morphological feature of the cavity affects resonance. In terms of building a sensor we are interested in improving sensitivity limits. A discussion of how sensitivity is defined in the context of whispering gallery mode sensors will automatically segue into how using BT is one path toward realization of a bio-complex sensor with amplified detection capabilities.

While optical modes have defined spatial dimensions, a key component of sensitivity is temporal; how long is an optical mode able to keep a photon bottled? A common metric to gauge a resonator's sensitivity is by determining its Q factor, what represents the energy stored versus energy loss rate. Formally:

$$Q \equiv 2\pi \frac{Energy\ Stored}{Energy\ Dissipated\ Per\ Cycle} \qquad \textbf{Eq. 3}$$

Another way of looking at this is through 'ring-down' times, τ. Resonators with a high Q will be able to store energy more efficiently, so if we were to stop driving the system, such a resonator would show a slower rate of decay of the energy stored inside. This would be considered a longer 'ring-down' time. For example, a resonator that oscillates at $\sin(\omega_0 t)$ with an energy decay rate proportional to $e^{-\frac{t}{\tau}}$ where τ = 10s and τ = 30s in another trial would display oscillation damping in the time domain as in Fig. 4.

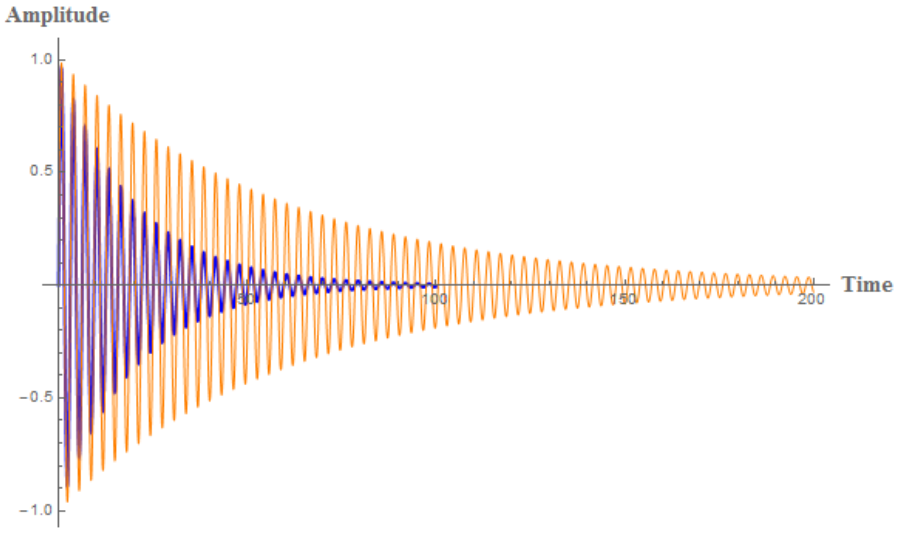

Figure 4: Time domain plot of two sinusoidally oscillating resonators with different ring down times. The orange plot represents a ring down time, τ=30s and the blue, τ=10s

Gauging ring-down times as a metric holds true for any resonator and might be related, somewhat more intuitively, to a measure of sensitivity by way of analogy. Imagine two pendula swinging back and forth, identical in all aspects except for a difference in their hinges that allows one to keep swinging after it's been perturbed for a longer time than the other (perhaps one is better oiled). Clearly, the pendulum with the longer swinging time has a lower rate of energy loss and thus a higher Q. One might reword the previous sentence to state that the pendulum with the longer ring-down time (read, swinging time) is simply more reactive to perturbations that alter the rate of energy loss and is therefore more '*sensitive'*. Whispering gallery resonators are no different, in that, a more 'sensitive' resonator will be more receptive to smaller perturbations in the state of the stored energy or rate of energy loss. In the case of bio-sensing systems, we will later discuss how a particle landing on the surface of the resonator will directly correlate with energy-related changes in the system.

A more useful definition of Q can be had when we realize the analogous plot but in the frequency domain, via a Fourier transform. We notice that the linewidth of a higher Q oscillator will be narrower.

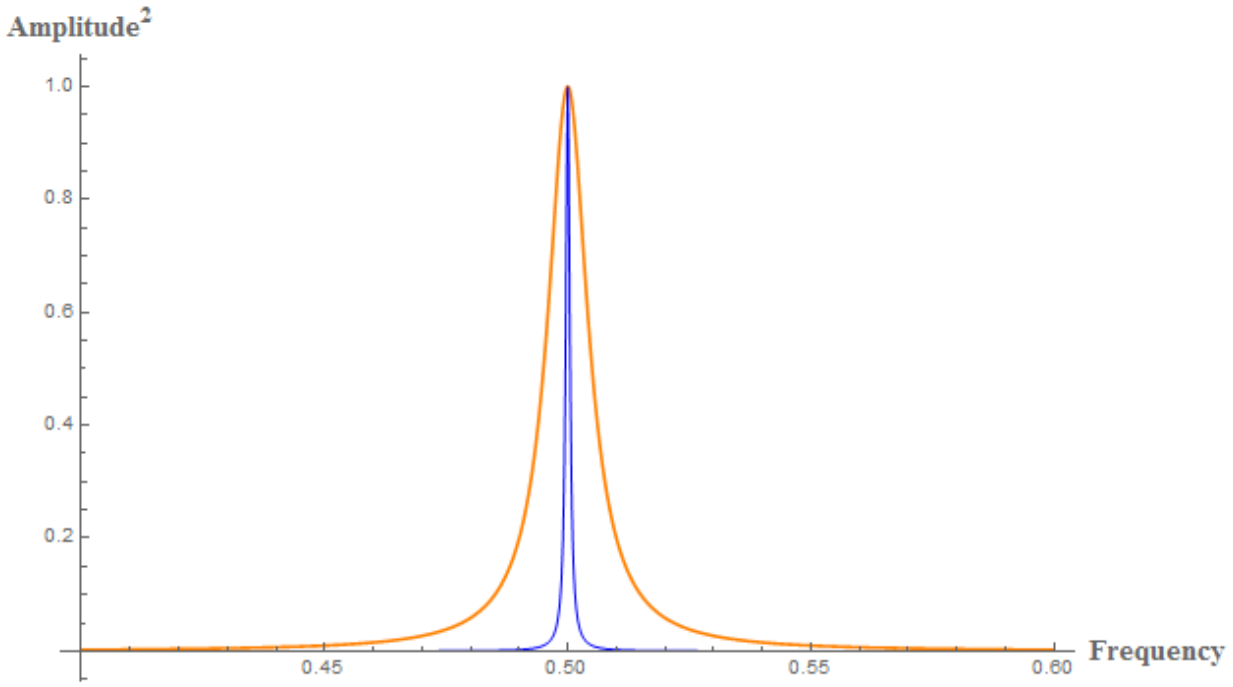

Figure 5 Frequency domain plot of two sinusoidal oscillators with damping coefficients, Γ = 0.01 Hz (orange) and Γ =0.001Hz (blue)

These functions resulting from the transform are called Lorentzians with the form:

$$\frac{\left(\frac{1}{2}\Gamma\right)^2}{(\omega-\omega_r)^2+\left(\frac{1}{2}\Gamma\right)^2} \qquad \textbf{Eq. 4}$$

where ω is angular frequency, ω_r is the resonant angular frequency and Γ is the damping co-efficient, or linewidth. Using this formality we can re-write Q as:

$$Q \cong \frac{\omega_r}{\Gamma} \qquad \textbf{Eq. 5}$$

Equation 5 is applicable to all resonators, including WGM resonators.

C. REACTIVE SENSING

For some time now it has been known that optical microcavities are capable of producing one of the most sensitive resonators to-date.[31] We've touched upon how changing the properties of the resonator can produce a shift in the properties of light circulating internally, however in order to create a sensor it stands to reason that perturbations to the light orbits on the inside will have to come from external particles. One way to begin understanding the effect of how external particles can affect the system can be to imagine, instead of increasing the radius of the resonator itself, adsorb a layer with thickness, t, to the outside.

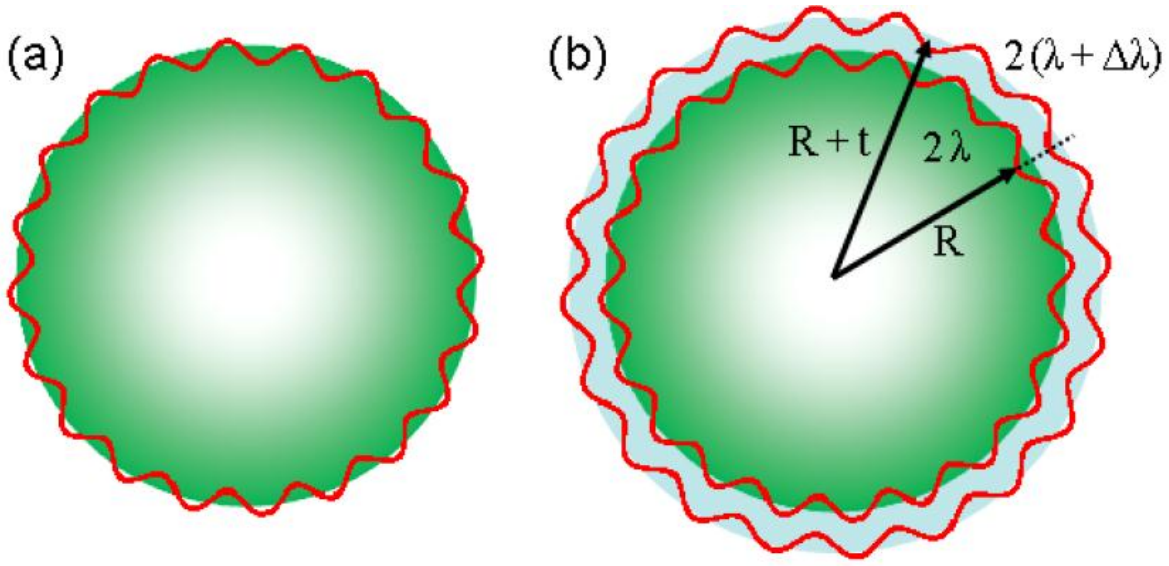

Figure 6: (a) Wave representation of the WGM, and perturbation – note that the wave penetrate beyond the dielectric boundary, this is the origin for the evanescent field. (b) Layer perturbation of the WGM, note that the wave moves outward, and the wavelength is extended to re-close the orbit in phase.

In order for the circulating light to return back in phase it must have an increased wavelength to accommodate for the circumference increase. Thus we will see the system react via a red-shift in wavelength. We can then immediately draw the relation:

$$\frac{\Delta\lambda}{\lambda} = \frac{\Delta t}{R} \qquad \textbf{Eq. 6}$$

Which would manifest itself on a plot as a shift in the center-point of a Lorentzian curve:

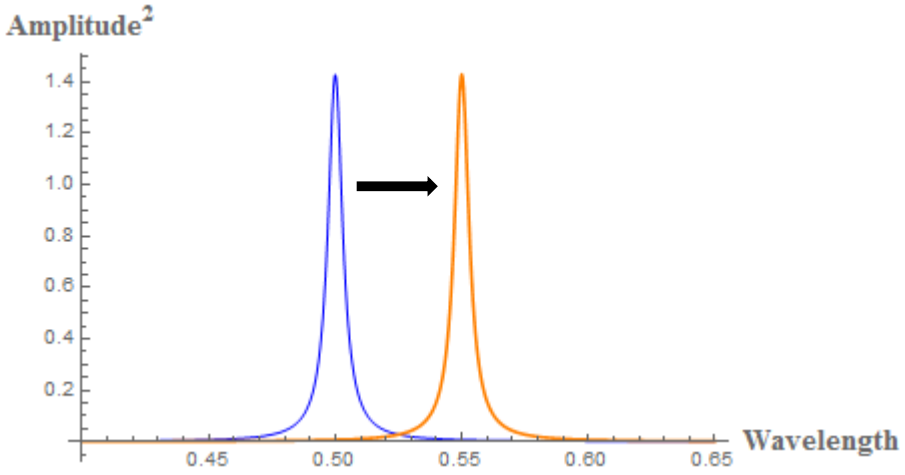

Figure 7: Shift in wavelength due to adsorption on the sphere surface

Thus the smallest particle layer detectable, given a Q of 10^6, of cavity diameter 20 μm at operating wavelengths of about 1μm would be able to detect adsorptive layers as thin as 20 picometers or 0.2Å!

D. EVANESCENT PROFILES

One might notice in Fig. 6 that the light circulating has a slight portion traveling outside of the sphere. While it is not to scale, this is, in fact, a physical representation of how light behaves at boundaries. The field traveling outside of the resonator is called the evanescent field – so called due to the fact that its intensity dies out approximately exponentially as one travels away from the surface of the sphere:

$$E(\underline{r}) \sim E_0(\underline{r})e^{\frac{-h}{L_E}} \qquad \textbf{Eq. 7}$$

where h, equal to r – R, is the interfacial distance; distance away from the resonator. E_0 is the field at the resonator surface and L_E is the characteristic evanescent length. This exponential decay of the field only applies over a finite distance from the resonator surface; indeed, whispering gallery mode resonances are 'leaky' because for reflection at a curved surface the confinement of the light is not absolute and trapped photons can tunnel out through the boundaries of the sphere and escape.

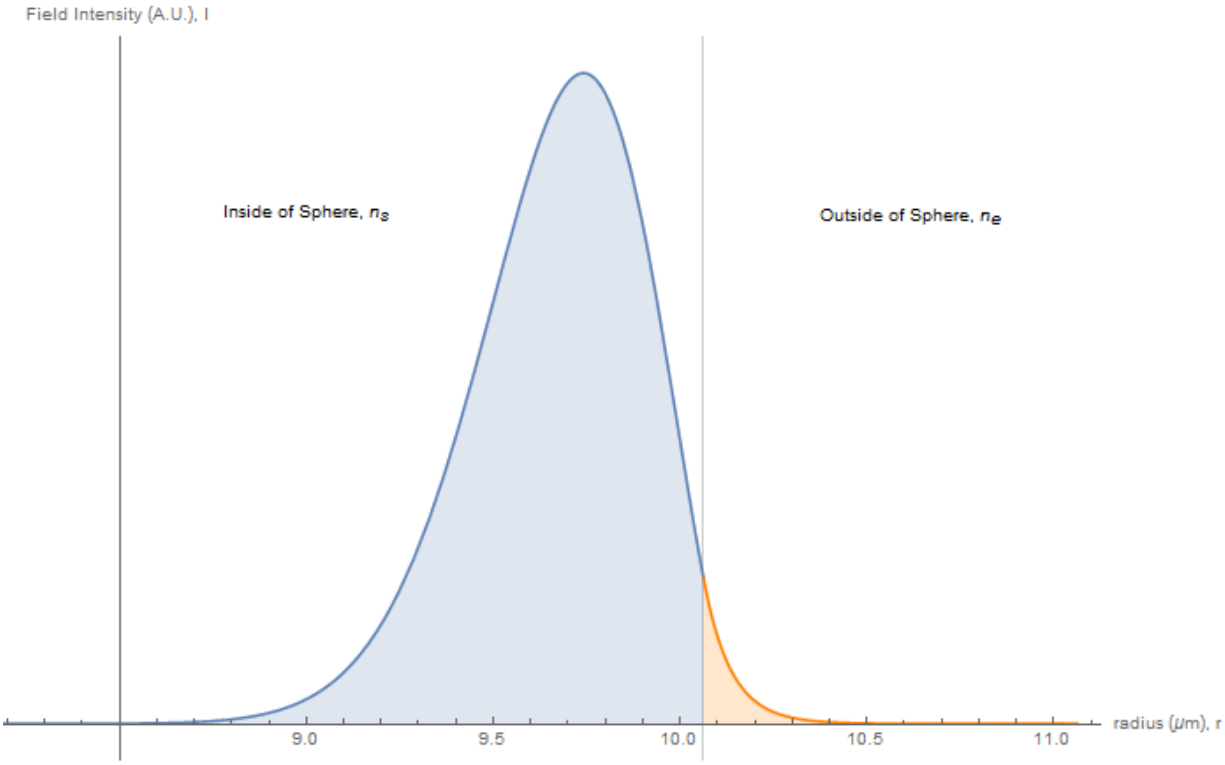

Figure 8: Representation of a typical first order field intensity split between the inside (blue) and outside (orange) of a spherical cavity. Vertical gray line denotes radius of the cavity.

Although small, the evanescent region (orange) is responsible for being able to couple light into the sphere from an external source and also forms the basis for sensing all external molecules. The length of the evanescent field is limited by imperfect TIR, in that photons are able to tunnel out. For a given wavelength of resonance the evanescent field does not continue to decay until infinity but instead only exists between the right-most edge of the potential well in Figure 3 (where r = R, that is the radius of the cavity) to some r outside of the cavity (r>R) that is defined by the edge of the potential curve. This is called the reactive region and is the radial limit of the external region where a particle's presence can influence the field inside of the cavity. Typically the length of the evanescent field can be characterized by fitting it to an exponential decay function (an approximation that is shown to work very well for first order resonances within cavities sizes where a 'grazing angle' of incidence approximation for light within is acceptable) and is generally metered by the distance away from the cavity surface (gray vertical line) at which the surface field intensity has dropped to 1/e of its original value.

E. SINGLE PARTICLE PERTURBATION

We have thus far shown that layer adsorptions acting as an increase in "effective" radius is a way to observe wavelength shifts. It is, however, necessary for bio-complex detection and single-molecule detection in general to be able to predict the perturbation due to a single particle.

The evanescent tail of the field induces a dipole moment in the particle in excess of the displaced water.[32] The polarization of the particle is associated with energy transfer to

the particle, via the evanescent field, where this energy comes from that stored in the resonator cavity. We may equate the transferred polarization energy on a single photon basis to:

$$\hbar\Delta\omega = -W_p \qquad \textbf{Eq.8}$$

$$where, W_p = \delta p \cdot \frac{E_0^*(r_i)}{4} = \alpha_{ex} E_0(r_i) \cdot \frac{E_0^*(r_i)}{4}$$

Here $\hbar\Delta\omega$ is the change in photon energy and $-W_p$ is the time averaged work due to polarization of a particle. The next set of equations assume W_p to be acting on a particle small enough to approximate as a single dipole, with excess polarizability α_{ex}. The fractional frequency shift due to an analyte particle located at position r_i is then represented by the ratio of the energy spent on polarization to the total energy within the resonator cavity. This is known as the Reactive Sensing Principle (RSP):

$$\frac{\Delta\omega}{\omega} = \frac{-W_p}{W_c} \qquad \textbf{Eq. 9}$$

Where W_c is the energy within the cavity. Written out it looks like:

$$-\frac{\Delta\omega}{\omega} = \frac{\Delta\lambda}{\lambda} \cong \frac{\alpha|E_0(r_i)|^2}{2\int \varepsilon_r |E_0(r_i)|^2 dV} \qquad \textbf{Eq. 10}$$

Here ε_r is the relative dielectric constant in the cavity, $\alpha=\frac{\alpha_{ex}}{\varepsilon_0}$ and V is volume.

This principle can be applied to all microcavity resonators and has the additional benefit of predicting reactive effect independent of intensity within the cavity since both numerator and denominator are proportional to the number of photons in the system. Therefore we will visit it again within the context of spheroidal cavities.

F. RESONANT MODE STRUCTURES

The reactive sensing principle has so far given us an idea of how particles can be detected, however we have not yet described how the various optical modes are constructed. The photonic atom, like the Bohr atom, has modes that can be parsed into four quantum numbers; angular momentum number *l*, the azimuthal angular momentum number *m*, the radial order number *n*, and the polarization *P*, (transverse electric TE or transverse magnetic TM). The goal of this section is to briefly show how morphology is linked to the *m*, and *l* mode resonant locations and how the polarization of incoming light can affect resonant mode locations as well. The *n* number for the duration of this section will be assumed to remain at one as it is known that *n* mode orders higher than one lead to significant Q degradation.

Since the orbiting light inside is guided by the periphery of the cavity it is a must to solve for the propagation of light at the interface of the cavity and its surrounding medium. For TE incident light the inner edge and outer edge of the boundary must have matching E fields (these fields only have tangential components for this system):

$$E_{in} = E_{out} \qquad \textbf{Eq. 11}$$

E_i (*i* representing either inner or outer) is directly proportional to ψ_r^i. Therefore the wavefunctions at the boundary must be matched as well ($\psi_r^{inner} = \psi_r^{outer}$). As it turns out, solving for the radial wavefunction, ψ_r, can be done by re-framing the Helmholtz equation in the form of a Ricatti-Bessel function and, written out, look like:

$$a_{in} n_s X j_l(n_s X) = a_{out} n_e X h_l^{(1)}(n_e X) \qquad \textbf{Eq. 12}$$

here, the left-hand side of the equivalence represents the wavefunction on the inside (for all radii less than or equal to the radius of the cavity, R) and the right-hand side represents the wavefunction on the outside (all radii equal to or greater than R). a_{in} and a_{out} represent amplitudes of the wavefunction. X is simply $2\pi R/\lambda_0$ re-dressed for ease as, what is called, a non-dimensional optical size. j_l and $h_l^{(1)}$ are the characteristic solutions to the Ricatti-Bessel function; the spherical Bessel function and the spherical Hankel function of the first kind respectively. Although this derivation is not trivial, it is not within the scope of this thesis to show how Eq. 12 was arrived at but rather at how it can be utilized.

A second boundary condition is given by having to, also, match the tangential component of the magnetic fields. This can be evaluated by using Faraday's Law in harmonic form, assuming the magnetic field to oscillate as $e^{-i\omega t}$. The boundary condition written in terms of the wavefunction show a familiar technique used in flow problems; continuity, which is expressed by taking derivatives of both sides:

$$a_{in}[n_s X j_l(n_s X)]' = a_{out}[n_e X h_l^{(1)}(n_e X)]' \quad \textbf{Eq. 13}$$

And finally bringing the two together we arrive at a transcendental equation for which we can solve for X, which contains the wavelength(s) necessary to meet resonant conditions:

$$\frac{[n_s X j_l(n_s X)]'}{n_s X j_l(n_s X)} = \frac{[n_e X h_l^{(1)}(n_e X)]'}{n_e X h_l^{(1)}(n_e X)} \quad \textbf{Eq.14}$$

It serves well later on to note that there is no amplitude dependence present in this equation and therefore resonance dependence on wavelength and refractive index is not dependent on the intensity of incident light. For TM mode incident light the boundary conditions are different but the resulting equation looks similar:

$$\frac{[n_s X j_l(n_s X)]'}{n_s X j_l(n_s X)}\left(\frac{n_e}{n_s}\right)^2 = \frac{[n_e X h_l^{(1)}(n_e X)]'}{n_e X h_l^{(1)}(n_e X)} \quad \textbf{Eq. 15}$$

This is perhaps solved most easily by finding the roots of the real part of the transcendental equation via numerical methods which can be expedited by feeding a Lam approximation in as a first guess.[33]

A sample of how the roots of the transcendental equations differ for TE and TM modes are plotted here for two identical resonators by the parameters, angular momentum

number l = 106, radial order number n = 1, cavity index of refraction n_s = 1.95 immersed in water with index of refraction n_e = 1.326:

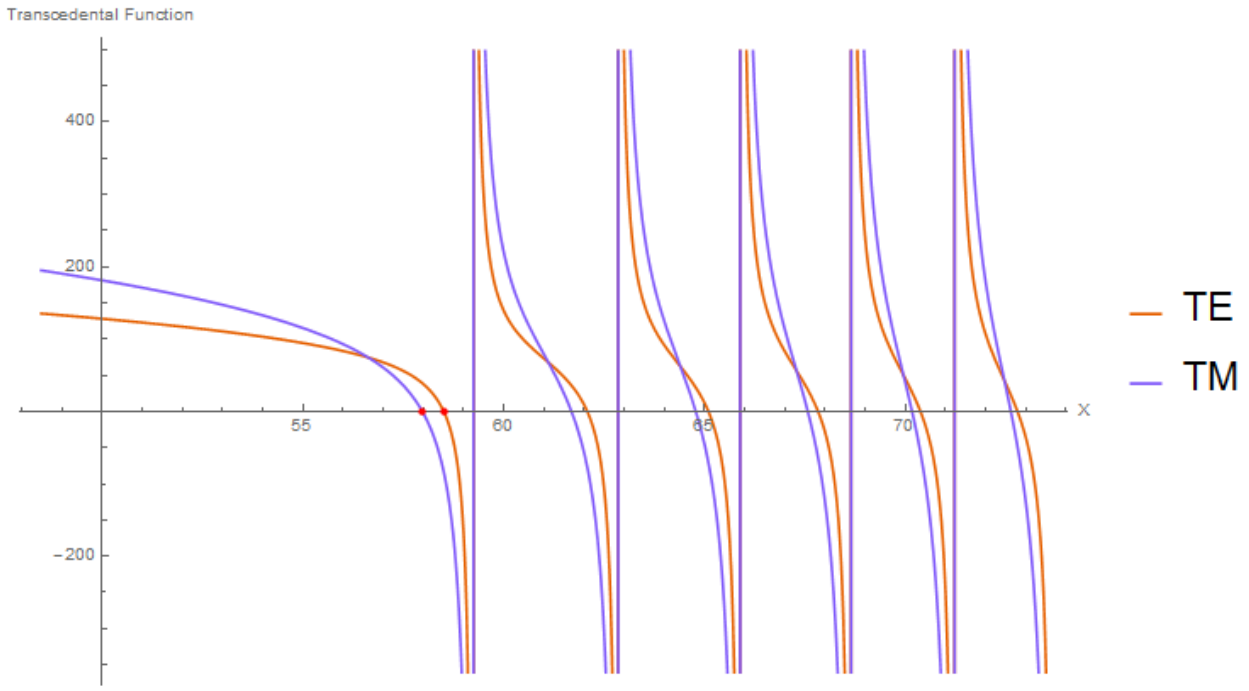

Figure 9: TE vs TM mode plot of the transcendental equation versus optical size, X. Orange represents TE mode, blue represents TM.

Qualitatively we are able to see that TE and TM resonances of the same l mode occur at slightly different X's. The TE root is at a higher X value and thus its wavelength of resonance is lower than that of TM.

We may also observe the dependence of X on different *l* numbers and refractive index of environment while holding the polarization constant (TE):

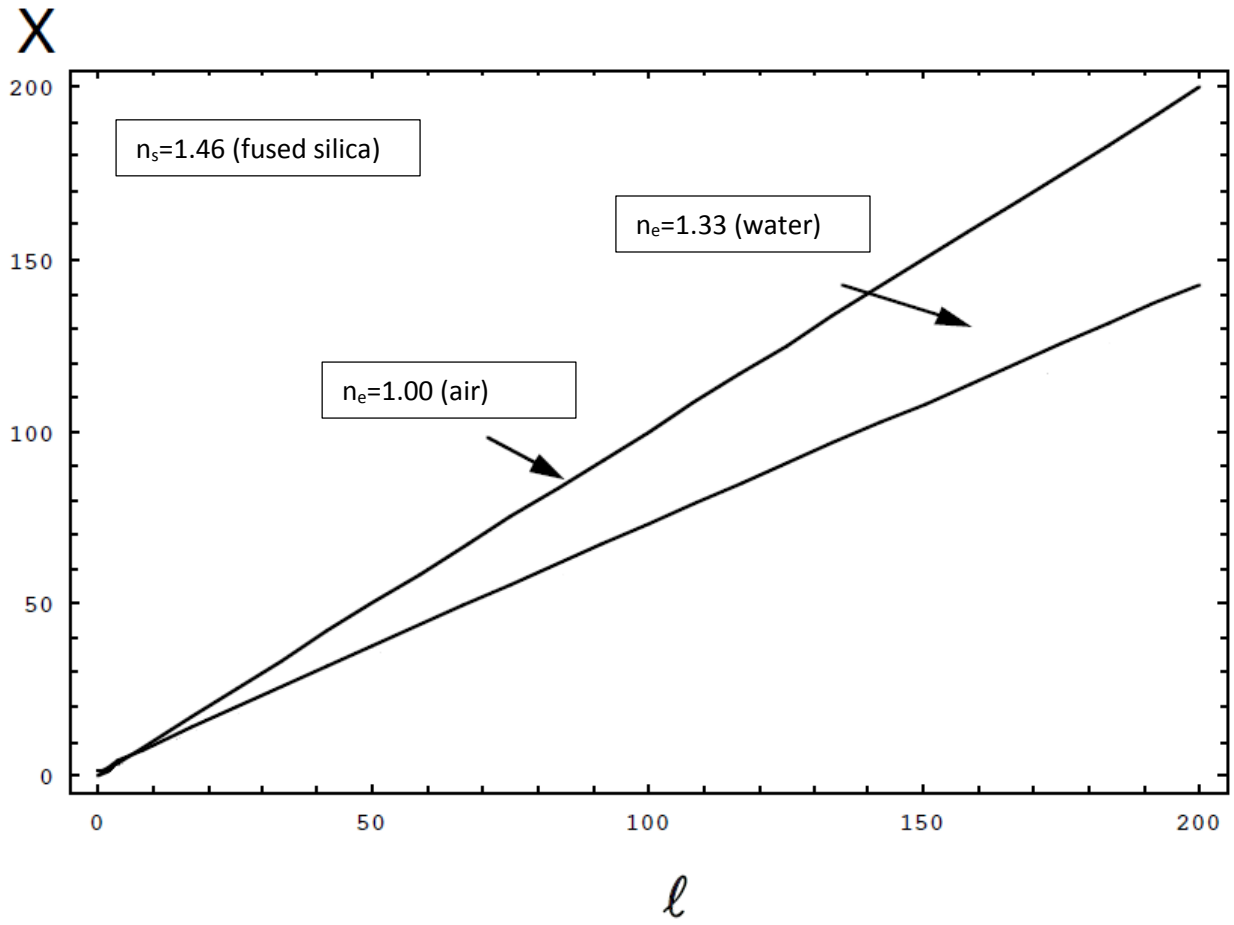

Figure 10: X vs. discrete values of l of a fused silica resonator immersed in two different media. Credit: Khoshsima, M. (2004)

Notice that for greater $n_s - n_e$ the slope of X vs. *l* decreases. It should make some intuitive sense that as refractive index contrast grows higher that light is less likely to seep out and thus should be confined better. Therefore, for an given *l*, it is not surprising that, X, the optical size for a cavity in air is greater than that of a cavity in water.

The azimuthal angular number, *m*, is the result of the z-component of the angular momentum operator, L_z,and holds an angular dependence if the resonator is not perfectly spherical.

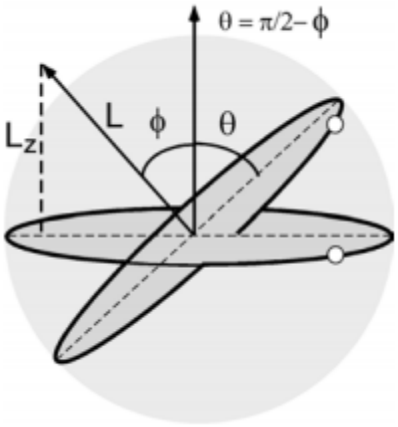

Figure 11: The L_z component, a projection of L, cannot vary along any φ or θ directions in a sphere since they all contain the same radius.

Fig. 11 shows that L_z is a projection along an axis of symmetry. In a sphere since all angles in the φ and θ directions are symmetrical all energy and momentum for any given *m* is the same. Thus, all *m* modes, which are allowed to range from *–l* to *l* are considered to be energetically degenerate.

However, in practice, eccentricity within a spheroidal object is unavoidable and therefore we do, in fact, see *m* mode splitting (lifting of the degeneracy). Due to its angular dependence, the further away from a perfect sphere the cavity is the further apart the *m* modes appear from each other. A given spectrum, with known *m* mode locations can be used to calculate a given resonator's eccentricity (or measure of a-sphericity). This is shown by modeling the spheroid resonance as the perturbation away from a perfect sphere of the same volume. The following steps of analysis are followed through by Young *et al.*[34]

by expressing the fractional shift in wavelength as some function of spherical distortion, sphere refractive index, optical size and the associated quantum numbers of the sphere:

$$\frac{\Delta\lambda}{\lambda} = \frac{1}{R_{sphere}} F\left(Y_M^L(\theta,\varphi); m\ n\ l\ \mu; n_s, X\right) \quad \textbf{Eq. 16}$$

Where μ represents either TE or TM polarized light. For physical spheroids (droplets in the case of Young *et al.*) some simplifications for distortion can be made given that they do not deviate too far from a perfect sphere. The distortion is assumed to be of the form[35]:

$$r(\theta,\varphi) = R_{sphere} + \Delta\sqrt{4\pi}Y_0^2(\theta,\varphi) \quad \textbf{Eq. 17}$$

Here, R_{sphere}, is the radius of a perfect sphere and the second term is the distortion away from it. Y_0^2 is a spherical harmonic function that ensures axial symmetry and a quadrupolar distortion of the sphere (pulling from one end and pinching at another in a way that ensures preservation of volume) and Δ is a uniform expansion factor.

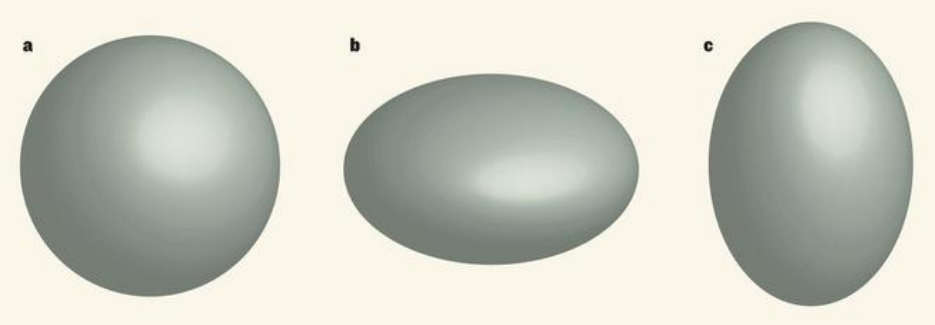

Figure 12: Quadrupolar distortions of a sphere, (a) perfect sphere (b) oblate spheroid (c) prolate spheroid

Given these simplifications, for TE polarized light inside of a prolate spheroid, the expression for *m*-mode shifts due to perturbations in geometry is:

$$\frac{\Delta\lambda}{\lambda} = 1 + \frac{e}{6}\left(1 - \frac{3m^2}{l(l+1)}\right) \quad \textbf{Eq. 18}$$

Where the eccentricity factor, *e*, is given by:

$$e \equiv \frac{r_p - r_e}{R_{sphere}} \quad \textbf{Eq. 19}$$

This can be used as a metric to estimate deviation away from sphericity. The veracity of such an equation can be confirmed by comparing to visual measurements of the resonator via microscope where the definition of R_{sphere} is taken to be the average of the prolate radius (major axis), r_p, and the equatorial radius (in this case the minor axis, but is generalized to mean the radial axis parallel to the incident beam of light), r_e.

In order to visualize the intensity of the modes in the microcavity we can map the field onto the sphere as a function of the spherical azimuthal and polar angles. The angular dependence of the field for spherical cavities can be described by spherical harmonic functions:

$$E_0(R,\theta,\xi) = \mathrm{a_{in}} \mathrm{j}_l(\mathrm{k_0\ R}\ n_s)\hat{\mathrm{L}}\ \mathrm{Y}_l^m(\theta,\xi) \qquad \textbf{Eq. 20}$$

Eq. 20 describes a transverse-electric (TE) field due to a single mode where a_{in} is the amplitude, $j_l(z)$ is a spherical Bessel function, $k_0 = \omega/c$, R is the distance from the center of the sphere and $\hat{L}$ is a dimensionless angular momentum (= $-i\mathrm{R} \times \nabla$) acting upon $Y_l^m(\theta,\xi)$, the spherical harmonic function. The mode index *l* is the number of wavelengths around the cavity equator, representative of the momentum of the photons circulating inside and the mode index *m* is the azimuthal momentum number that can take on values from –*l* to *l*, with each corresponding to a different spherical harmonic eigenfunction.[36],[37]

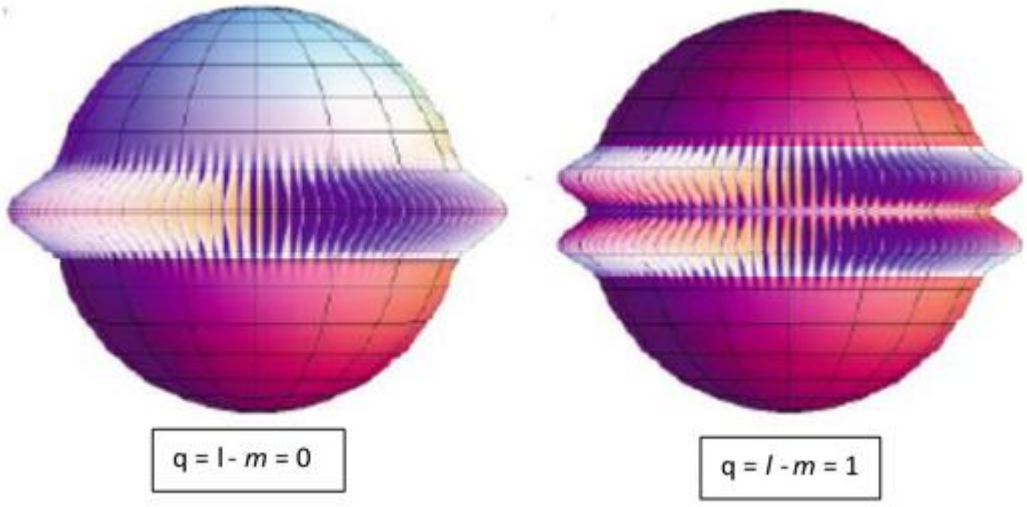

Figure 13: A depiction of q = 0 and q = 1 intensity distributions on a slightly elliptical sphere.

As discussed before the eigenmodes of a perfectly spherical resonator are energetically degenerate, however, slight asphericities can lift these degeneracies and cause different q ($q = l - m$) modes to resonate at different wavelengths. If then, the modes are sufficiently separated (that is, the resonant linewidths, as reflected in the quality factor Q, are narrower than the separation between different m-modes due to asphericity) scanning over two or more modes would yield a distinct resonant wavelength for each. The shift of a particular mode in response to particle binding will then depend on how strong the intensity of that mode is at the location where the analyte rests on the resonator surface.

The angular dependence of modes is not included in this thesis but readers may refer to[31] and see that the linewidth can be derived by finding the imaginary root of the transcendental function (not shown). Though the derivation isn't shown it is still worth pointing out that the coefficients of both the real part of the transcendental equation (wavelength profile of a mode) and the imaginary part (linewidth) are pieces of the Lorentzian denominator that define the resonant structure of oscillating systems.

G. LATITUDE LOCATION

The latitude locator is an essential feature of the microspheroidal resonator that was introduced in 2014 by Keng *et al*[38], however, one must first go back and apply the RSP to spheroidal geometry (Eq. 10), a resulting approximation that assumes a roughly spherical shape leads to the expression:

$$\frac{\Delta\omega}{\omega} \cong \frac{-\alpha|\mathrm{Y}_l^m(\theta,\xi)|^2}{(n_s^2 - n_e^2)R^3} \quad \textbf{Eq. 21}$$

where n_s and n_e are the refractive indices of the surface cavity material and surrounding medium respectively. (note: applicability of this equation drops off quickly further away from *m=l* depending on the sphericity of the resonator). This equation applies to a mode interacting with an assumedly, dimensionless, point particle. A modification was done in order to accommodate a particle with a finite volume. This leads to introduction of a form factor, g(z), as the overlap integral between the surface normalized evanescent intensity and volume elements of the particle divided by the volume of the particle[36]:

$$\frac{\Delta\omega}{\omega} \cong \frac{-\alpha|\mathrm{Y}_l^m(\theta,\xi)|^2 g(z)}{(n_s^2 - n_e^2)R^3} \quad \textbf{Eq. 22}$$

Where g(z) is:

$$g(z) = \frac{6}{(2z)^2}(1 + e^{-2z}) - \frac{12}{(2z)^3}(1 - e^{-2z}), where\ z = \frac{a}{L_E} \quad \textbf{Eq. 23}$$

This form factor correction works so long as g(z) is always near 1, meaning that, *a*, the radius of the particle should be much lower than, L_E, the evanescent length.

For any polar angle that a particle lands on, ξ, there will be a distinct amount of overlap of the particle with each mode that it perturbs and the amount of overlap will perturb that mode proportionally.

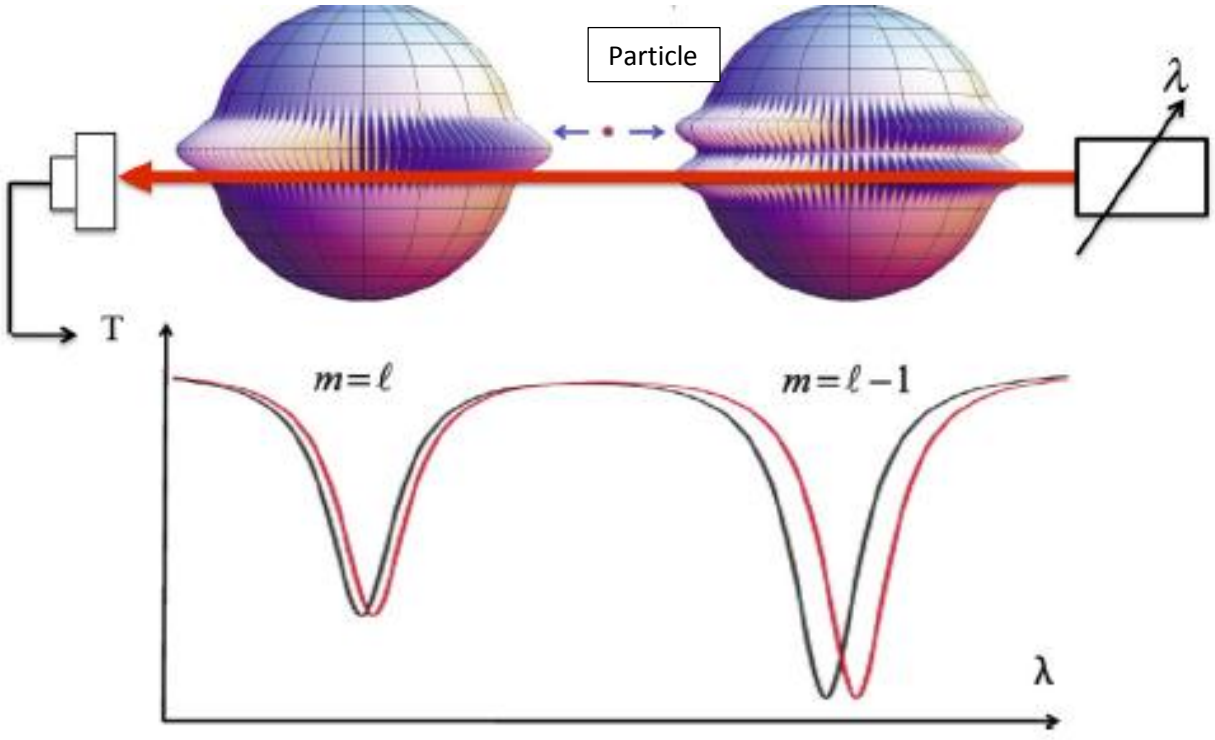

Figure 14: Polar modal intensities of a slightly prolate micro-spheroid excited by a spectral laser scan. The particle adsorbed north of the equator (red dot) has a larger overlap with the intensity of the q = 1 mode (right) and as a consequence that mode shifts to a greater extent.

Re-writing the RSP-predicted shift in terms of wavelength instead of angular frequency leads to:

$$\Delta\lambda \cong \frac{\alpha|\mathrm{Y}_l^m(\theta,\xi)|^2 g(z)}{(n_s^2 - n_e^2)R^3}\lambda \qquad \textbf{Eq. 24}$$

From which we can compare the shifts of two modes by taking a ratio:

$$\frac{\Delta\lambda_{l,l-1}}{\Delta\lambda_{l,l}} = \frac{\left|\mathrm{Y}_l^{l-1}(\xi_p)\right|^2}{\left|\mathrm{Y}_l^{l}(\xi_p)\right|^2} \quad \textbf{Eq. 25}$$

this shows that the latitude, ξ_p, of the particle can be found independent of its physical properties and can be conveniently extracted by transforming the spherical harmonic functions into Hermite-Gauss asymptotic expressions: [28]

$$\frac{\left|\mathrm{Y}_l^{l-1}(\xi_p)\right|^2}{\left|\mathrm{Y}_l^{l}(\xi_p)\right|^2} \approx 2(l-1)\xi_p^2 \quad \textbf{Eq. 26}$$

Combining Eq. 24 & 25 gives the absolute latitude:

$$\left|\xi_p\right| = \sqrt{\frac{1}{2(l-1)}\frac{\Delta\lambda_{l,l-1}}{\Delta\lambda_{l,l}}} \quad \textbf{Eq. 27}$$

Which can also then report back particle size in a single binding event by re-expressing Eq. 24,

$$a^3 g(z) \approx \frac{(n_s^2 - n_e^2)R^3}{\left|\mathrm{Y}_l^l\left(\frac{\pi}{2}, \xi\right)\right|^2 D_\alpha} \frac{\Delta\lambda_{l,l}}{\lambda} \quad \textbf{Eq. 28}$$

where

$$D_\alpha = \frac{4\pi n_e^2\left(n_p^2 - n_e^2\right)}{\left(n_p^2 + 2n_e^2\right)} \quad \textbf{Eq. 29}$$

where n_p is the refractive index of the analyte particle.

H. INTRODUCTION OF LIGHT FORCE ASSEMBLY

Light Force Assembly (LFA) is the result of combining ideas within the last few sections. As was discussed earlier, the analyte within a mode volume is polarized in proportion to the squared modulus of the mode's electric field. Due to the exponential decay of the evanescent field the portion of an analyte closer to the surface of the microcavity is polarized more strongly than parts further away. The resultant gradient of polarization creates an uneven pull on the particle toward the radial direction of the microcavity. This effect was previously utilized by Keng *et al.*[39] to produce an orbital motion of the particle around the cavity dubbed 'carousel motion':

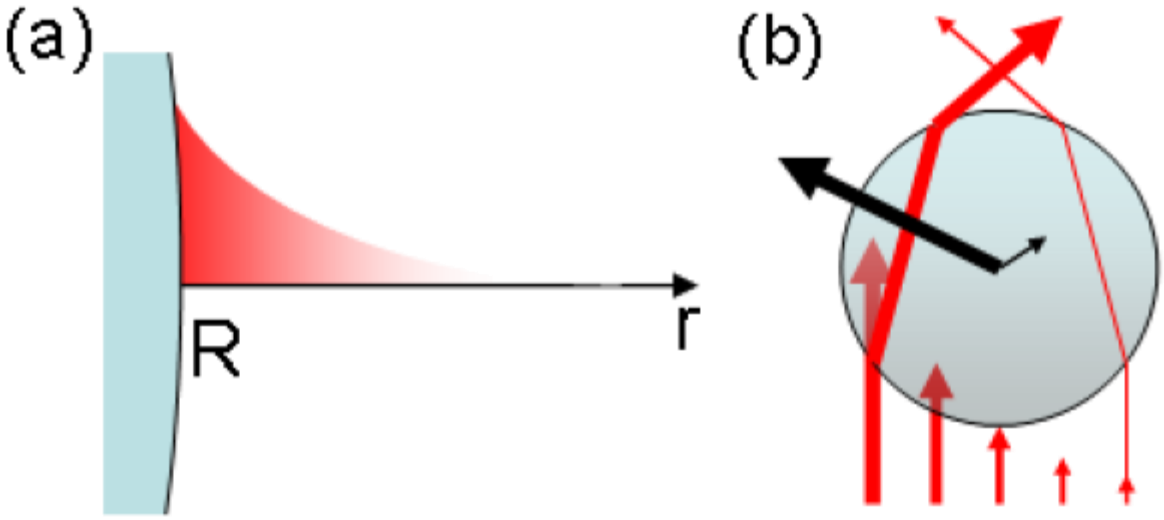

Figure 15: Left, evanescent field protruding from the surface of the cavity creating a gradient force (right) upon a nearby particle. The black arrows depict the parity in force vectors toward and away from the surface of the microsphere.

The pictured system above shows a ray-trace depiction of the light imparting a greater momentum flux nearer to the microsphere surface. An analyte particle of diameter 500 nm would 'feel' a gradient pull of a resonator with evanescent field length of around 200nm proportional to:

$$F(r_i) \propto \left(\frac{e^{-\frac{r_1 - R}{L_E}}}{e^{-\frac{r_2 - R}{L_E}}} \right) = \left(e^{\frac{500nm}{200nm}} \right) \approx 12 \qquad \textbf{Eq. 30}$$

That is it would feel 12 times the force at its point nearest to the microsphere compared to its furthest. However, in Keng *et al.*[37] it was seen that a particle would not simply come near to and 'sit' on the microsphere surface as one might expect and that rather it rapidly fluctuated in the radial direction while in orbit. An analysis of this yielded:

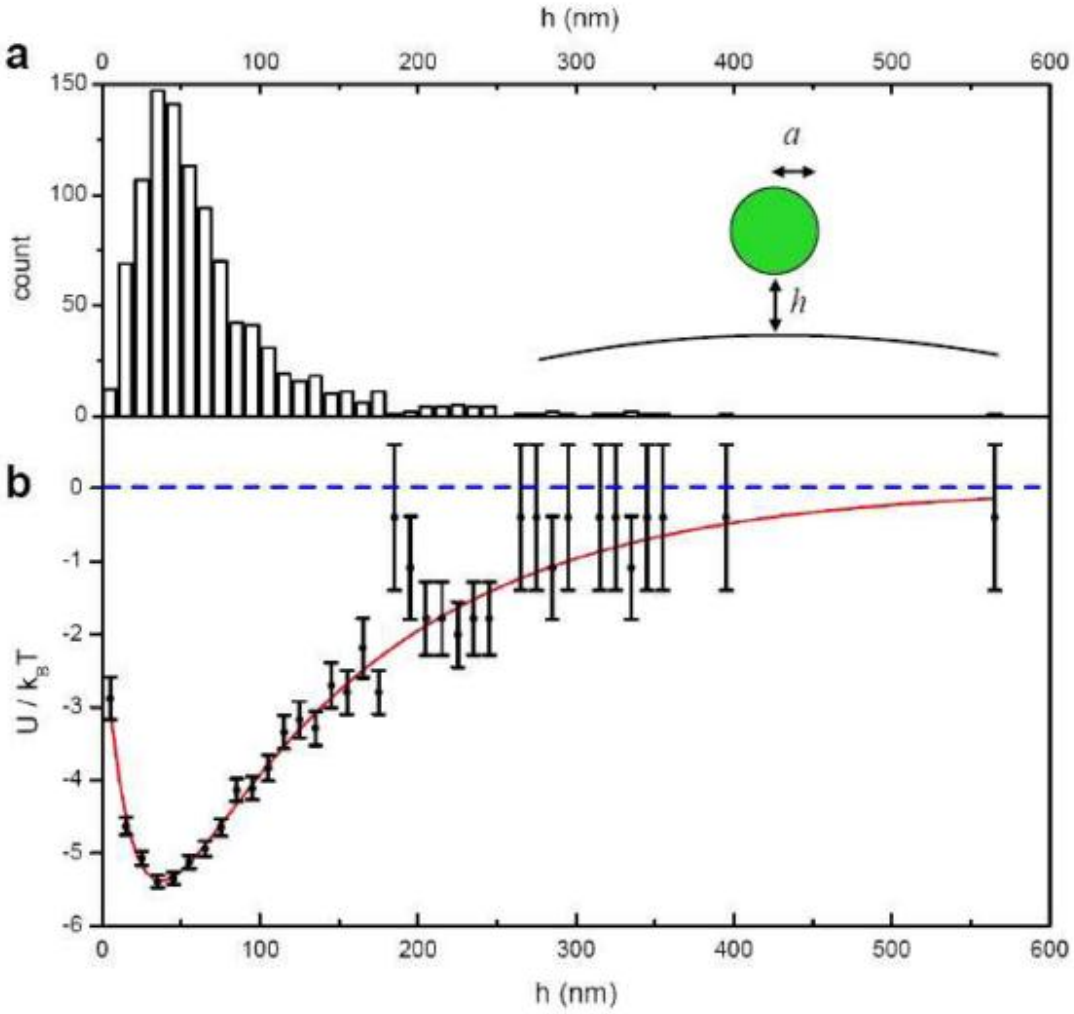

Figure 16: Separation histogram and trapping potential. (a) separation histogram collected from a single trapping event of a polystyrene particle (from mean radius <a> =140 nm hydrosol). The WGM with Q = 7.3E+5 was excited with P = 233 µW at λ ≈1060 nm in a microsphere with R = 44 µm. The statistics were comprised of 1000 points. (b) Potential plot arrived at from the histogram in (a).

The picture that evolved was a particle that was being pulled out of a Brownian walk by the optical light forces, in a similar manner to that of trapping by optical tweezers, and then being pushed away as it neared the surface of the microsphere due to a repulsive Debye layer. This was confirmed by the red line shown above, which was

modeled by balancing the long-ranged, "polarization potential" of the light forces around the sphere, U_p, with the short-ranged, Debye potential, U_s:

$$U(r,P) = U_p(r,P) + U_s(r) \quad \textbf{Eq. 31}$$

The interesting feature of the model shows that an imbalance can be created by modulating the driving power of the incident light, P, as the Debye potential is not affected by it. The Debye potential, rather, results from the chemistry of the bare silica surface of the microcavity which contains ionized silanol groups in water at pH 7; repelling any negatively charged particles (in the case of the above graph, polystyrene).

The Debye potential can be visualized as a global 'force-field' that extends radially outward from the surface of the cavity characterized by the Debye length, λ_D:

$$\lambda_D = \frac{2z^2e^2n_\infty}{D\epsilon_0 k_B T} \quad \textbf{Eq. 32}$$

z represents the valence number of any symmetrically valent salts (e.g., z = 1 for NaCl). e is the elementary charge, n_∞, is the bulk solution salt concentration, ϵ_0 is the permittivity of free space, k_B the Boltzmann constant, T the temperature of the solution and D the dielectric constant for the solution (which can be approximated as the dielectric constant of the *solvent* given that the salt concentration is sufficiently low).

Any particles further away than the Debye length are shielded from any electrostatic repulsion by an intervening salt solution and any particles within the Debye length see a charged surface and interacts with it. We know, from previous work,

the characteristic length of the evanescent fields to be in the range of about 100 to 200 nm, in comparison it is of interest to calculate the Debye length for typical WGM systems. In water, at 25°C, for low concentrations of a single monovalent salt the interaction length is estimated as[40]:

$$\lambda_D = \frac{0.3044}{\sqrt{C_{bulk}}}\ nm \qquad \textbf{Eq. 33}$$

Where C_{bulk} is the molar bulk salt concentration which yields a length in units of nanometers. Thus, a sodium chloride concentration of 0.001M would produce a Debye length of 9.62nm. Fortunately as we have just learned, in order to avoid repulsion we can simply increase the salt concentration to screen surface charges.

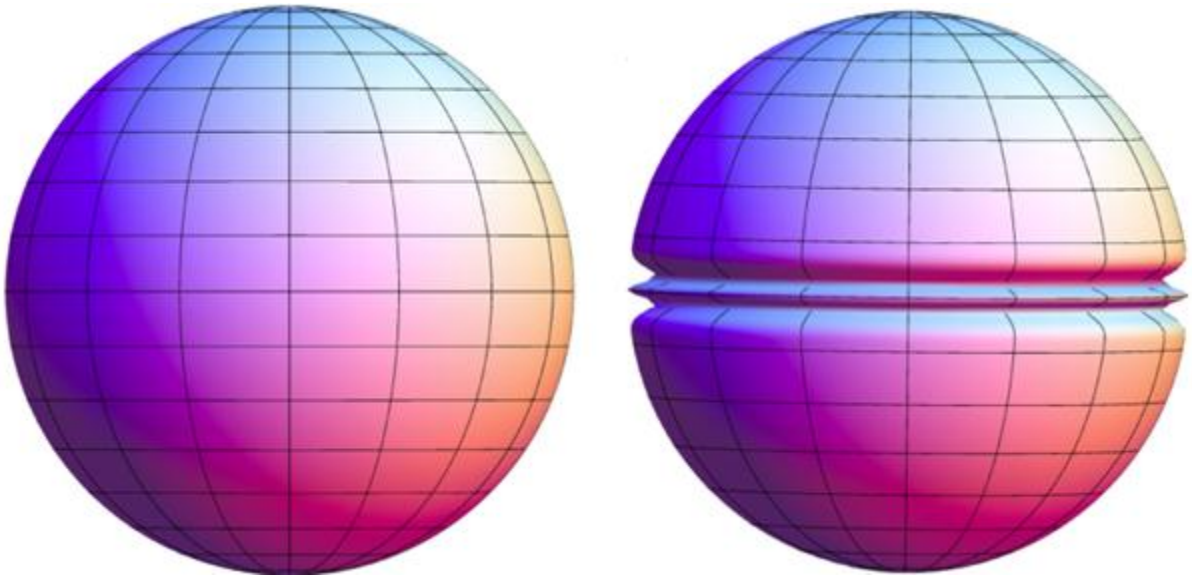

Figure 17: Left: Resonator shielded by a global Debye potential field. Right: *l-1* optical mode cutting through the field creating trenches for particles to settle into.

With an increase of power and salt concentration it is easy to imagine a system where particles can simply be pulled down to the surface of the resonator. A sum total picture of the LFA process can be visualized by optical light forces carving out trenches

in the surrounding Debye field creating potential wells that allow particles to fall out of solution into a narrow region on the resonator.

For angles close to the equator of the sphere we may roughly quantify the potential of both the attractive and repulsive force:

$$U(r,P,\xi) \cong -A\left|\hat{\mathrm{L}}\,\mathrm{Y}_l^m(\xi)\right|^2 QPe^{-\frac{r-R}{L_E}} + Be^{-\frac{r-R}{\lambda_D}};\ r > R \qquad \textbf{Eq. 34}$$

Here, the first term is the attractive potential, U_p, where Q is the quality factor, P is driving power controlling the strength of the field, the exponential represents the approximate intensity profile of the evanescent field outside the sphere at a distance measured from the center of the particle being pulled in, r, from the edge of the sphere, R. The co-efficient, A, is positive and contains fixed morphological parameters for the cavity and particle it interacts with:

$$A = \frac{\alpha_{ex}}{\omega\,({n_s}^2 - {n_e}^2)R^3} \qquad \textbf{Eq. 35}$$

α_{ex} is the excess polarizability of the nanoparticle and ω is the frequency of light.

The second term is the repulsive potential, U_s. The profile of a Debye potential is a solution of the Poisson-Boltzmann equation that can be approximately represented by an exponential term which holds true when the electrostatic potential is small ($\ll k_BT$).

The co-efficient B is positive and represents the surface potential as a function of the Debye length and is governed by the number of interacting species and their geometry.

As more power is injected into the cavity, the potential falls down below $-k_BT$ so that spatial trenches on the surface of the microsphere represent significant energy wells for particle capture. A particular set of trenches can be accessed by varying the frequency of the laser to activate the corresponding *m*- mode; thus, particles can be effectively placed at various latitudes with near nanometer precision.

It is well known that nano-plasmonic enhancing epitopes used in conjunction with WGM sensors have proven to be among the most sensitive label-free detection methods available to the field of bio-sensing. However, this requires the assembly of plasmonic particles on the surface of the WGM microsphere. LFA offers a simple, cheaper and more time efficient alternative to lithography techniques, with comparable precision.

III. EXPERIMENTAL SET-UP & LFA

This section introduces the reader to experimental equipment and methodology necessary to understand how results were obtained and how they were justified. Additionally many aspects of this thesis come from experimental complications involved in trying to manipulate micro-scale systems.

A. EXPERIMENTAL SET-UP

1. Materials

Resonators were made out of amorphous materials of two kinds for this thesis. Silica glass resonators were made from fused glass optical fibers and were used for the LFA experiments while commercially purchased barium titanate spheres (Corbeads4-N-N™, Corpuscular Inc., NY, USA) were used to explore higher refractive index cavities for eventual use in biosensing. Light was evanescently coupled into resonators via a flame tapered Corning® SMF-28™ single mode optical fiber and typically done under de-ionized (DI) water as a solvent. A 1064 nm distributed feed-back laser (E0037162, EM4 Inc.) was used as the incident light source with an isolator within a Mark-I™ unit (MP3Laser, MA, USA).

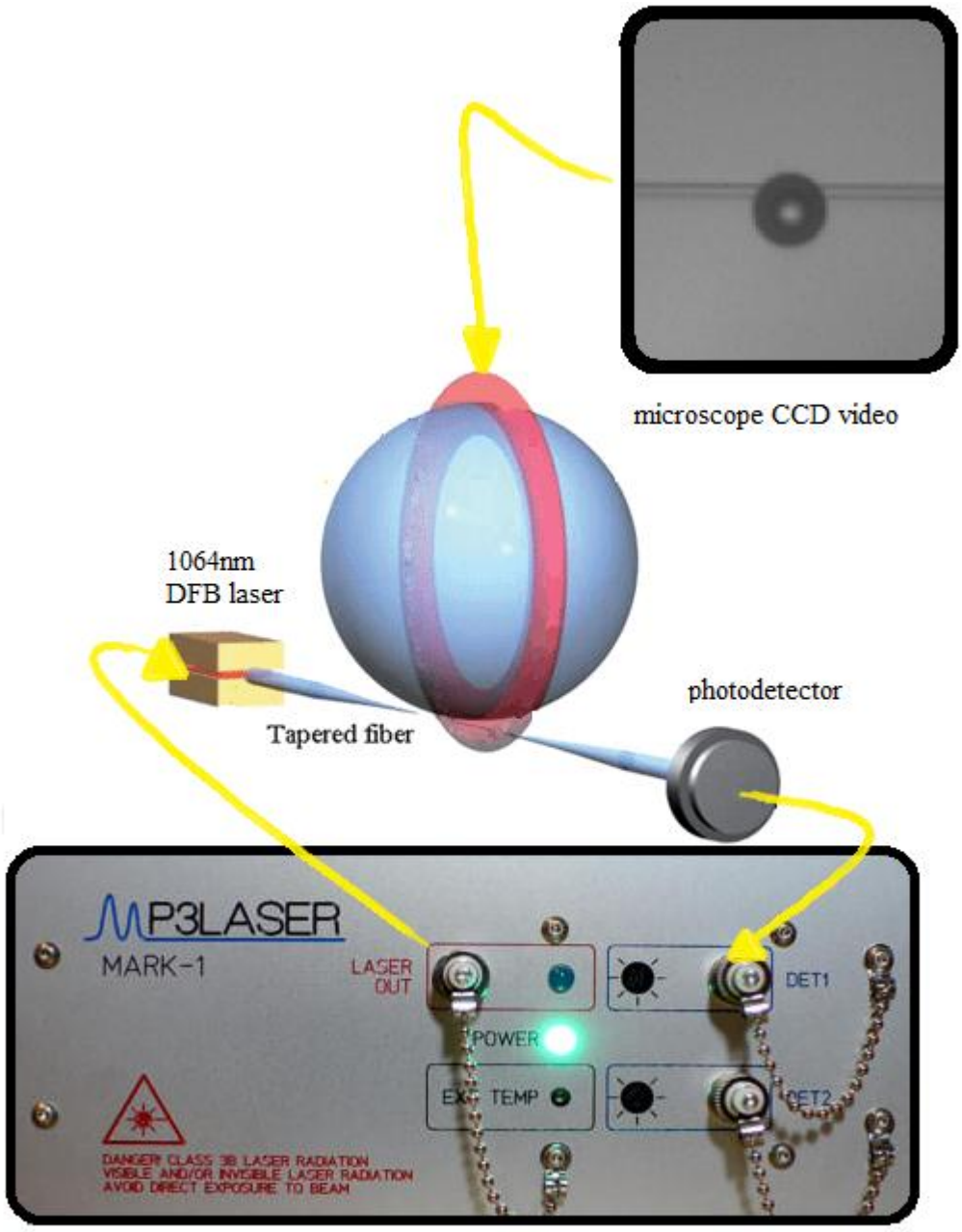

Figure 18: WGM tapered fiber-microsphere system connected to the Mark-I. Optical attenuator and polarizers not shown. CCD video picture is that of an approximately ~20µm barium titanate sphere resting atop a ~4-5µm optical fiber

2. Overall System Assembly

The Mark-I drives the 1064nm DFB laser via a current sweep which sends a scan of wavelengths into an optical fiber via a connectorized port pictured above (‘Laser Out’). The light travels through an in-line variable optical attenuator (Oz Optics Inc.) which allows up to 30dB attenuation of the light and then runs through in-line wave plate polarizers (Phoenix Photonics Inc.). The light travels through a thinly tapered section of the fiber, above which a spheroidal resonator is positioned. Light traveling through a taper is exposed evanescently outside of the fiber which is then coupled into a cavity mode (pictured in red). Above the resonator a microscope lens captures a bird’s eye view of the system. As light enters the resonator a characteristic glare (leakage of light at tangents) can be seen coming out of the resonator. The tell-tale sign of coupling to a resonant mode is the intensifying of this glare which can be explained by re-calling that light builds up at resonance and therefore the leaked light is also of greater average intensity.

The information that is collected by the photo-detector, however, is not the light intensity of glare spots but instead measures the intensity of light coming through the other end of the tapered fiber. Without the presence of a resonator, the intensity of light reaching the detector (DET1; an InGaAs detector) is simply a flat line. With a resonator there is generally a noticeable drop in this baseline which is due to the collection and subsequent leakage of light by the cavity. At resonance light is able to circulate through the cavity and re-enter the tapered fiber; this light has been transmitted once into the cavity and once back out and as a result is phase shifted by 180°. As a result it destructively interferes with the light going through the fiber and creates a loss of signal at the resonant wavelength. This is pictured as a ‘dip’.

3. Fiber Assembly: Flame Tapering

The basic structure of a bare SMF-28 single mode fiber has three main components, a Germanium doped silica core, a slightly lower refractive index silica cladding and an acrylate polymer coating.

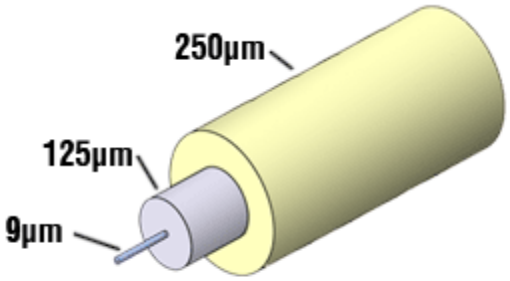

Figure 19: SMF-28 single mode bare fiber cross section view. Composed of three layers (1) 9 µm core (2) 125 µm cladding (3) 250 µm jacketing.

Picture courtesy of CablePlus[41]

Light traveling within an optical fiber carries a characteristic intensity profile dependent upon the geometry it travels through much like velocity profile for fluids in channels. Unlike fluids, however, part of the light is allowed to travel outside of high refractive index channels. In order to expose more of this light the fiber is thinned down, or tapered, which then is used as a way to couple light into an external cavity such as a microsphere.

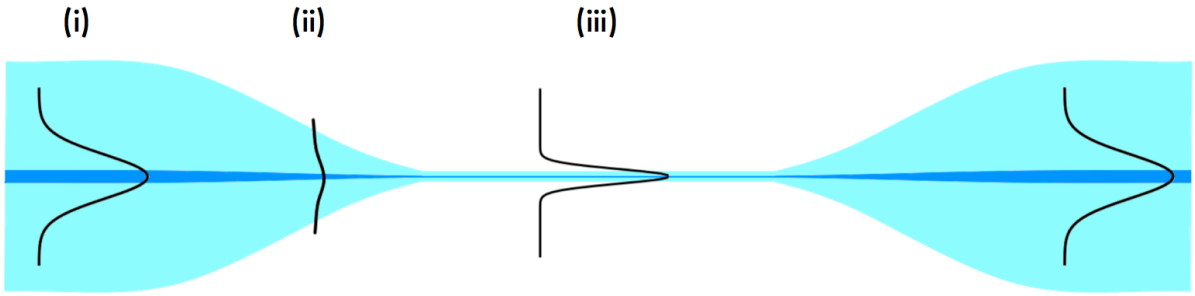

Figure 20: Representation of light traveling through a tapered optical fiber (not to scale). (i) Untapered region, light mostly travels through the core and partly through cladding (ii) Mid taper region, more of the light begins to travel through the cladded portion (iii) Thin taper region, most of the light is traveling through cladding and outside of the fiber

Picture courtesy of Center for Quantum Information and Control[42]

In order to begin tapering, the polymer coating is first stripped off with standard optical fiber strippers. In this thesis flame tapering was the method of choice, done with an apparatus designed by Dr. David Keng. The flame is produced by a propane / oxygen mixture which burns at approx. 1200°C. The mixing ratio is controlled by mixing valves which then send the gases into a narrow micro-nozzle that allows for a small flame:

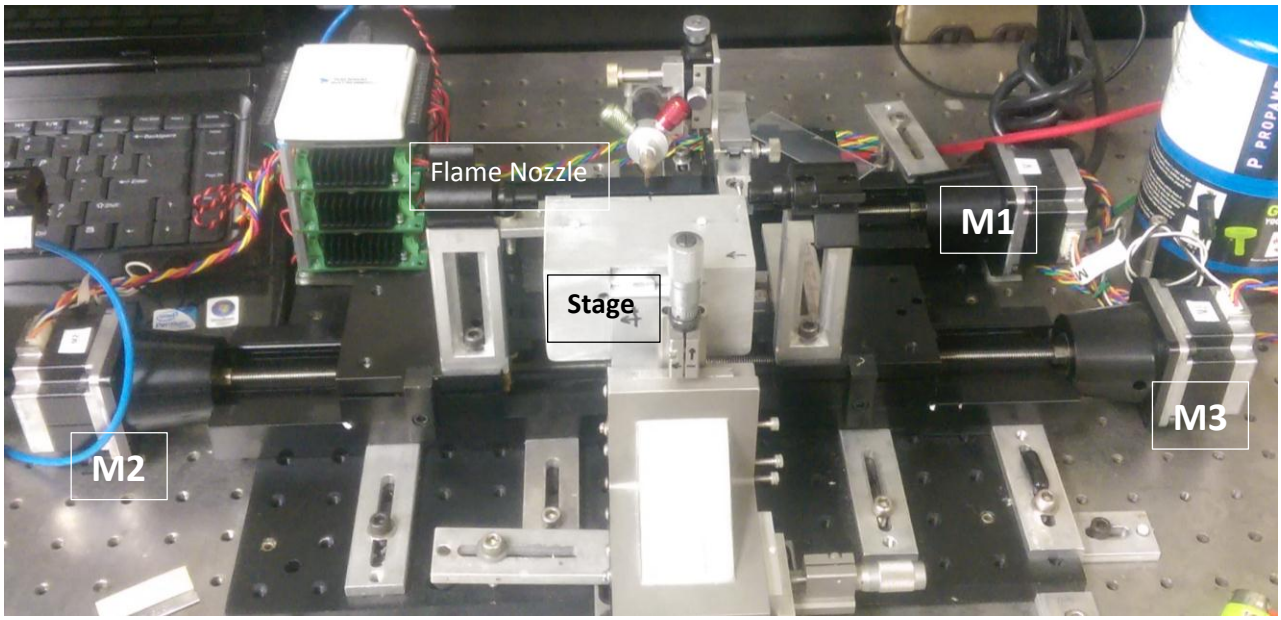

Figure 21: Flame tapering station. A stage to hold the slide sits under a micro-nozzle that emits oxygen (green knob) and propane (red knob). The stage is flanked by two fiber grips which are pulled by the two linearly actuated motors (M2 & M3). The flame nozzle is swept over a 3mm portion of the fiber to ensure that an even heating region is maintained. This is done with M1. All three motors are connected to a micro-controller which is manipulated through a LabVIEW™ GUI (not pictured).

As is pictured, the fiber is laid over the flame nozzle and held in place by two fiber chucks. Each chuck is pulled opposite each other by linearly actuated motors operated via a LabVIEW™ GUI interfaced with a microcontroller.

4. Fiber Assembly: Mounting to a support

The fiber was tapered and then mounted onto a standard microscope glass slide (75mm by 25mm and 1mm thick) which serves as a mechanically rigid support. The slide is pre-spotted with CYTOP™ (Asahi Glass Co., LTD.) which is an amorphous fluoropolymer that can serve as a non-hermetic channel blockage (via its hydrophobicity) thereby allowing atmospheric pressure equalization within the microchannel.

This glass slide is then placed on top of a pre-aligned stage designed to work with the microchannel and microscope assemblage in the lab. This stage is positioned under the tapered fiber which is then lowered carefully onto the glass slide until the polymer jacketed regions at both ends are resting on the slide.

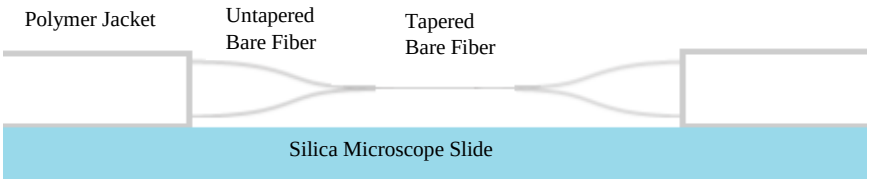

Figure 22: The tapered portion of the fiber is propped away from the glass slide by the jacketed regions

Proximity of the tapered region of the fiber to the glass slide would result in a significant loss of light via coupling into the slide.

The jacketed regions are then affixed to the slide by NOA 81™ optical adhesive; curable with a 365 nm UV-lamp (Spectronics Corp., 5" tube) within one minute.

5. Microfluidic Cell

As was discussed in the section above, CYTOP™ needs to be applied to the glass slide in order to serve as fluidic blocks to prevent seepage into unwanted areas of the microfluidic cell and eventually out of the cell entirely. The cell is designed to be affixed to the slide *after* the tapered fiber is affixed to the slide. The need for such a cell is to be able to do experiments within aqueous environments but at the same time be able to

replenish or supply solvent/solutes to the system in a manner that does not require any disassembly.

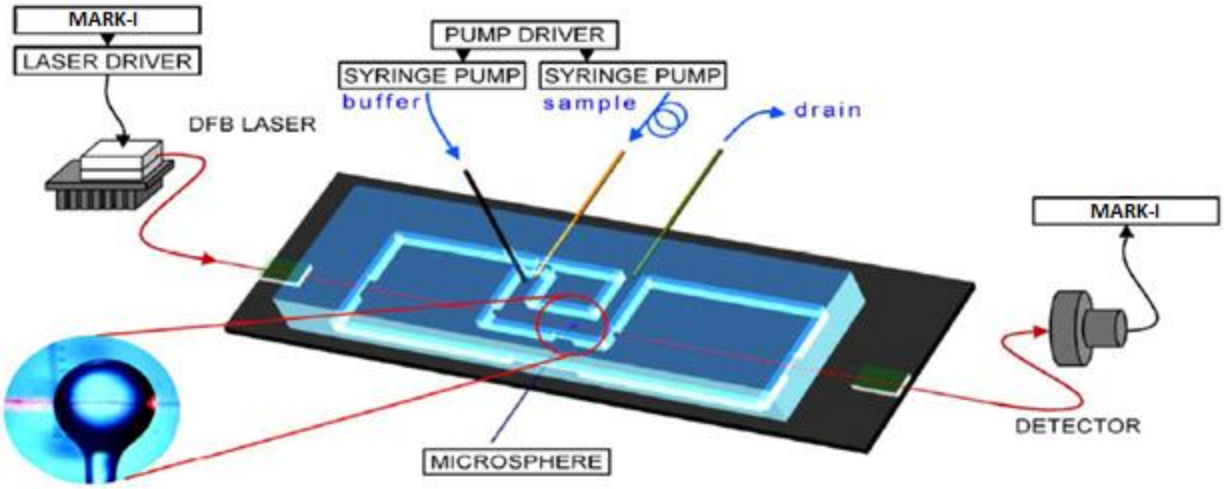

Figure 23: Sketch of microfluidic cell and all of its input and output ports for fluids and fibers.

The cell is made out of cross-linked polydimethylsiloxane (PDMS) and serves as a "cap" for the glass slide with carved ports and channels (pictured by the light blue edges above). The fiber (in red) is sent through a dedicated channel with enough clearance so as not to touch the fiber; each of these ports are sealed with CYTOP™. The microsphere (blue) also has its own dedicated channel through which it can be fed into the channel via a stem (talked about in the following section); these channel ports are also sealed with CYTOP™. Lastly two input ports for fluid are shown. Syringe needles are fed into the inlets which are hooked up to syringes that deliver the solute/solvent into the "U" shaped microchannel. The microchannel holds about 200μm from end to end until the fluid reaches the drain which is a syringe needle hooked up to a vacuum pump in order to ensure that no back-logs occur.

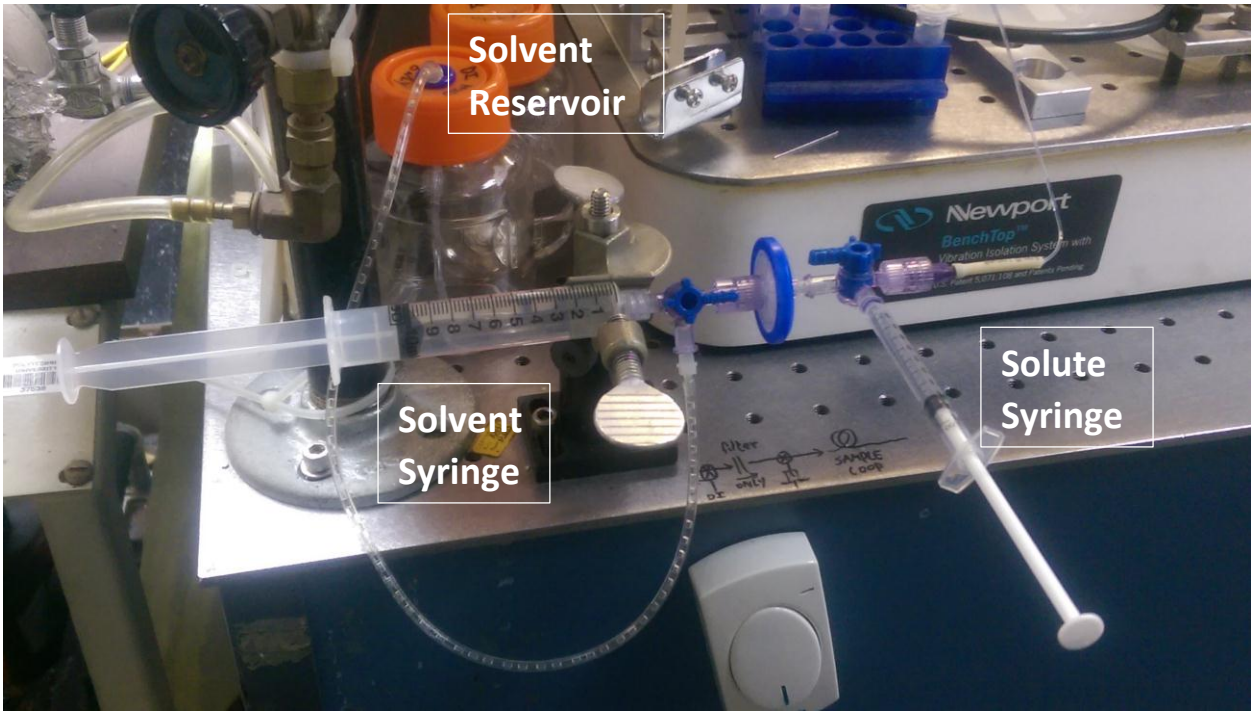

Figure 24: A picture showing an easy-to-operate sample delivery system made with a series of syringes and tubing. The solvent syringe draws up to 10mL and then is able to be pushed through a filter and into the sample loop where it meets the solute syringe (1mL syringe). One can be operated while the valve to the other is shut off and vice versa.

Each PDMS cell is made by temperature curing a commercially bought PDMS (Sylgard 184) within a mold designed by Dr. David Keng.

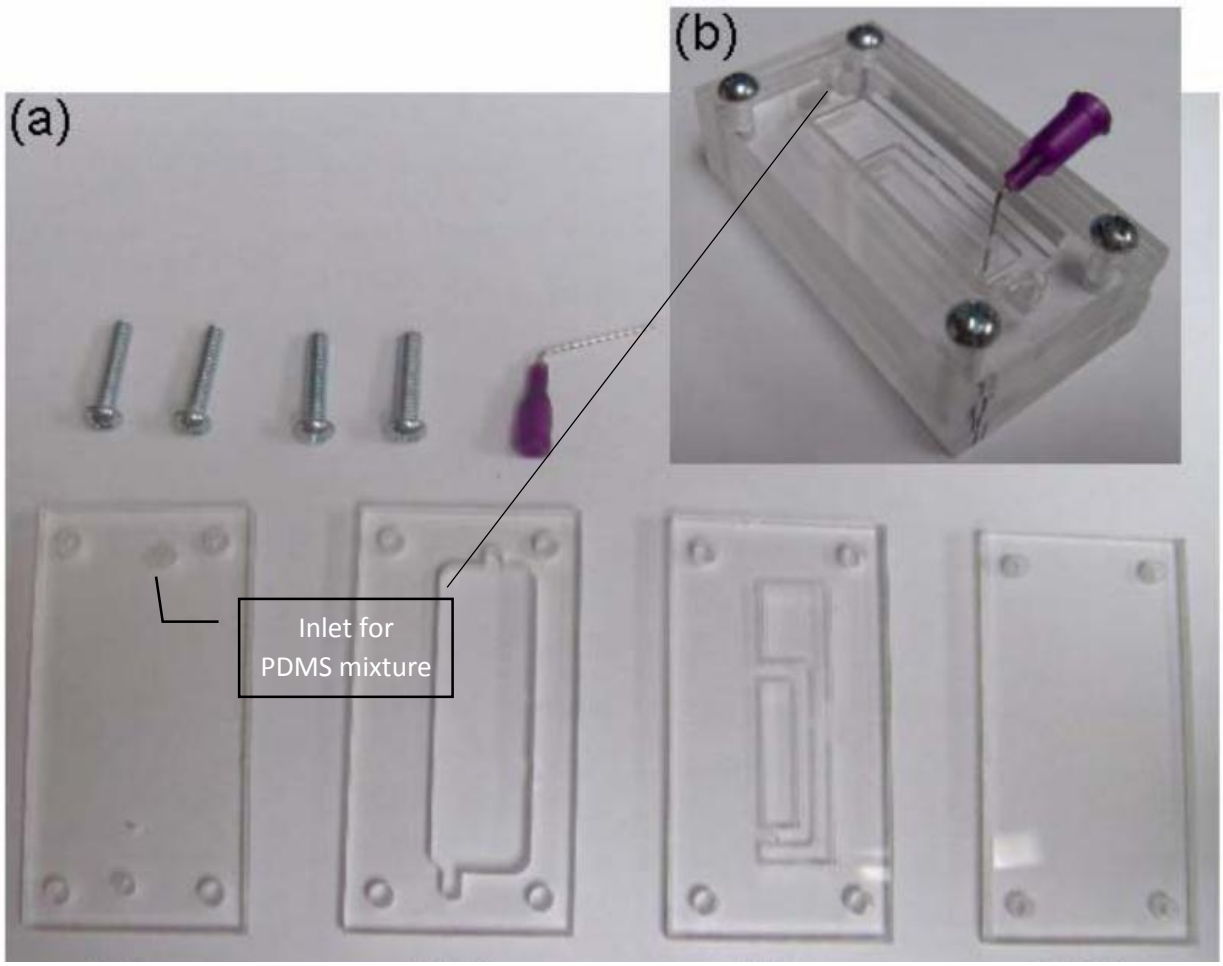

Figure 25: (a) an exploded view of the mold and all of its pieces (b) master mold, the screws hold the four layers together and the purple syringe needle serves as a spacer to allow for the formation of a buffer inlet port. The black line shows where the PDMS mixture is flowing into via a 60mL syringe

The master mold is assembled by stacking each of the four pieces one on top of the other (the right most piece is the bottom layer and each piece subsequently to the left gets stacked on top to create what is seen in Fig. 25 (b). The process involves mixing a 10:1 ratio of polymer:catalyst (both from the Sylgard 184 kit) inside of a 60mL syringe. The mixture is

then de-gassed via weak vacuum to minimize the presence of air bubbles. The mixture is flowed into the fully assembled master mold and allowed to sit for about five minutes airing out any excess bubbles left remaining within the mold chamber. After bubble removal the mold can be left at room temperature for about 3 hours or can be temperature cured at 70°C for 1 hour. After curing the mold is unscrewed and the PDMS cell can simply be 'peeled' out of the middle two layers.

6. Silica Microsphere Fabrication

In order to create a silica microsphere, an optical fiber tapered *end* was heated above melting point, after which surface tension of the melted silica naturally forms a spheroid. The heating was done via a 10μm CO_2 laser spot heating; training the laser onto the fiber end via a ZnSe lens. The light attenuates quickly managing to penetrate only 30 μm into the silica causing uneven heating (leading to asphericities). Since there is no mechanism to rotate the fiber stem a reflector was added on the other side of the fiber in order to minimize uneven heating.

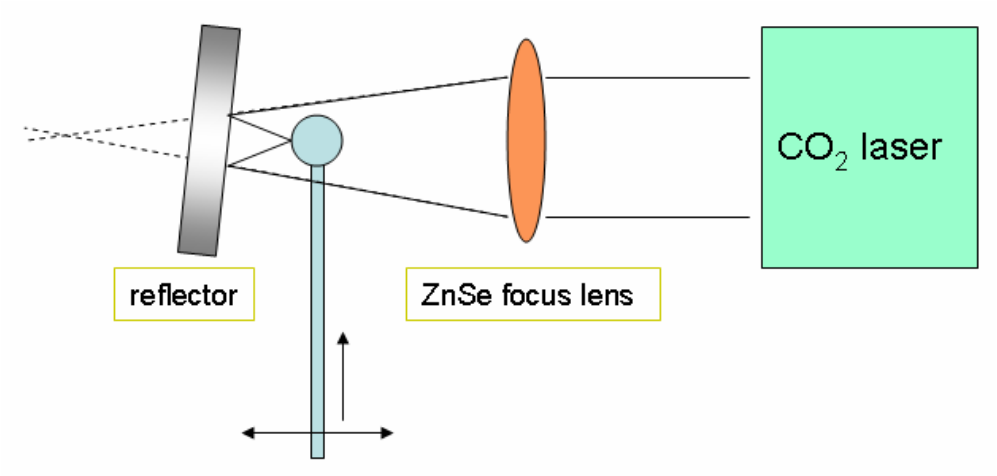

Figure 26: Silica microsphere fabrication assemblage.

This is monitored in real time by a CCD camera placed above the fiber that allows a qualitative, bird's eye view measurement of sphere size. The fiber is controlled by an XYZ stage that is used to deliver the fiber into the heating region of the laser beam. This way the size of the sphere can be controlled by feeding more or less of the fiber in.

7. Microscope and Microscope Stage

The fiber-on-slide is then set onto a stage directly underneath a microscope objective turret and a nearby XYZ stage which maneuvers the silica resonator into position to couple with the waveguide fiber. The ends of the waveguide fiber are connectorized and joined to a laser output port of the Mark-I on one end and on the other end into a detector port. The stage, which holds the slide has a Peltier thermoelectric module underneath (used to control the temperature of the buffer environment), also has controls allowing it to be raised, rotated and moved for the purpose of alignment.

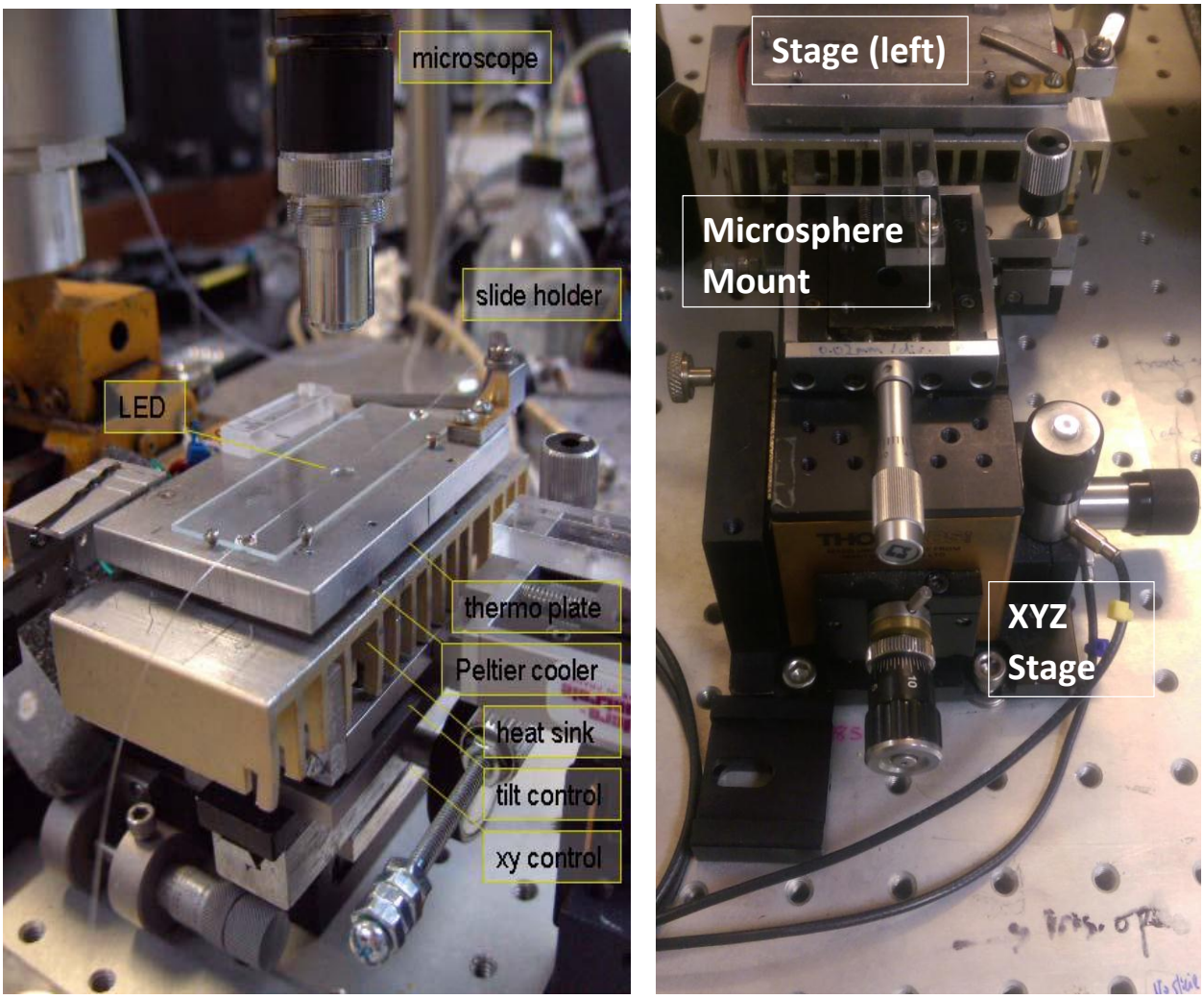

Figure 27: Pictured on previous page. Left: Fiber-on-slide assemblage atop microscope stage. Right: XYZ stage control and mount for guiding silica resonators attached to an optical fiber stem which is placed in the groove (small PDMS piece behind "Microsphere Mount")

Additionally, an inline variable optical attenuator and polarizer were inserted between the laser output of the Mark-I and the fiber-on-slide. The polarizer is composed of two quarter-wave plates and one half wave plate, the combination of which are used to isolate either a TE or TM mode during experiments. The optical attenuator often serves as a good way to be able to couple a minimal amount of light into the system which is beneficial in scenarios where binding is not wanted (either at all or perhaps is wanted later).

Additionally, too much power delivered can often create undesired non-linear behaviors as we will see later on.

8. Structure of Output Data

The Mark-I comes with its own customized software that enables the user to read detector outputs and manipulate laser control.

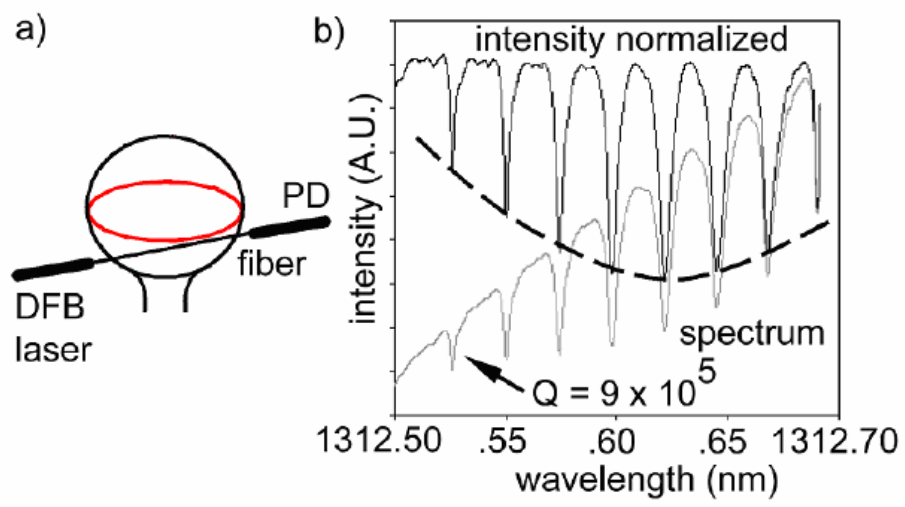

Figure 28: Waveguide excitation of a WGM, and typical spectrum of many WGM dips. WGM orbit represented by ring inside the spheroid.[43]

Figure 28 shows a simplified diagram of both the coupled silica resonator-fiber system and corresponding data output. The observable 'dips' represent different m modes being excited by a continuous laser scan and are in the form of an inverted Lorentzian function. An uncoupled (no resonator) system scan would show a straight line and a subsequent coupling scan would show an inverted peak, or dip, due to resonant light within the microsphere destructively interfering with the light within the fiber thereby diminishing the amount of photons sent into the detector.

The following is a screenshot of a Mark-I software interface:

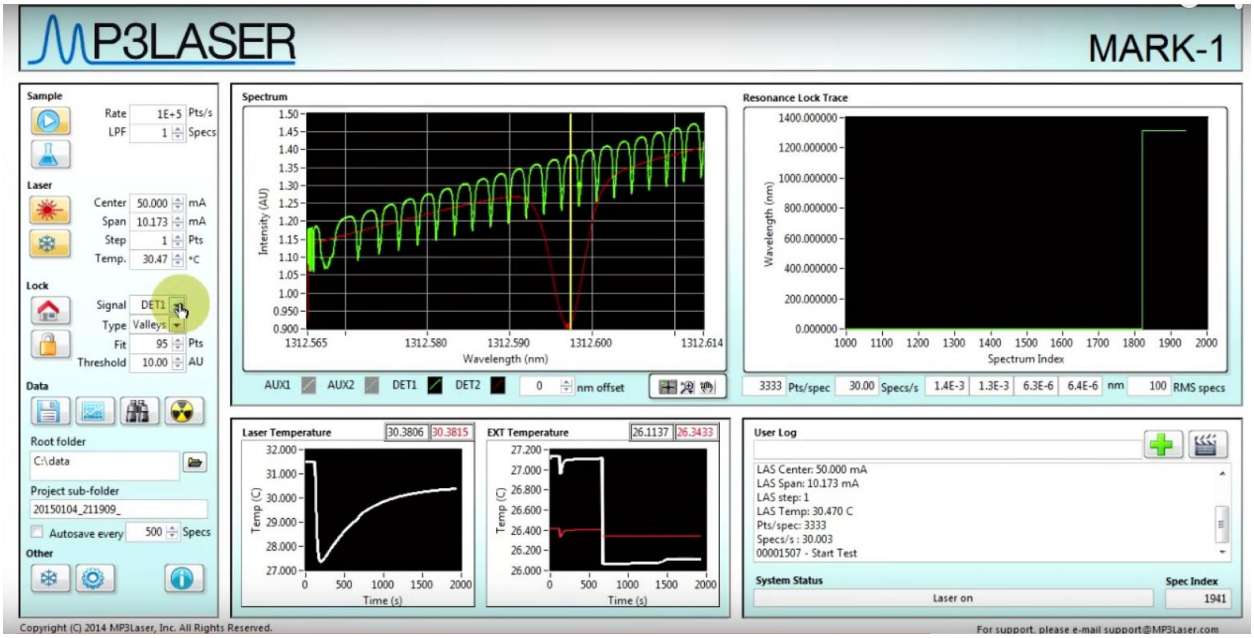

Figure 29: Spectrum window displays the resonances of a 50cm WGM ring resonator in green and the absorption line of an HF atomic cell in red.

The software features laser manipulation controls from scanning current ranges to temperature control. A scan window is featured in the center and to its right is a wavelength shift graph which is able to take a 'locked-on' dip point and track it continuously. Sampling rate can be varied as well. The bottom right has the option to record any notes the user may be interested in documenting and the entirety of all this data can be saved in excel friendly formats for later analysis.

IV. LFA EXPERIMENTS

The LFA experiments were approached with the hypothesis that particles could be reliably landed into the sensing region of one mode by increasing the optical power to it. Although definitive proof of the principle has not been demonstrated, preliminary evidence so far suggests that the concept does work as intended. What is required now is data that more clearly elucidates the phenomenon; this is all discussed within this section.

A. METHODOLOGY

Building upon past experiments proving the hypothetical question, of whether a mode is able to pull a particle to its sensing region reliably, can seem to be a straight forward matter of drawing in a particle using a single mode and then sweeping the laser over a range of modes to use the latitude locator and confirm the particle has or has not bound to the expected polar angle. Unfortunately this task is not so simple. Proof of drawing in and binding a particle in real-time is required. That is, confirmation that no other forces have acted upon the particle from single mode scanning to multi-mode scanning, or perhaps that the particle is not moved around while on the surface by the switching to multi-mode scanning.

Thus the first experiment done toward this goal was to simply scan two modes (the lowest number of modes required to use the latitude locator), the $m = l$ and $m = l\text{-}1$ modes. These two modes were chosen due to restrictions on the latitude locator that require near-spherical polar angles to work that exist only near the equator of the resonator.

The particles used in this experiment were commercially bought polystyrene (PS) 457 ± 11 nm in diameter (Polybead®, Polysciences, Inc.) within one standard deviation. A 25,000x dilution-by-volume of particles was created in a 30mM NaCl buffer, from a stock concentration of 2.84% solid. This was done by sonicating the stock solution for 20 minutes before diluting and then allowing the mixture to return to room temperature. A roughly 83μm diameter silica resonator was used and the following TE polarized spectrum was observed with a laser current centered around 85mA with approximately 300μW of power being delivered through the tapered fiber:

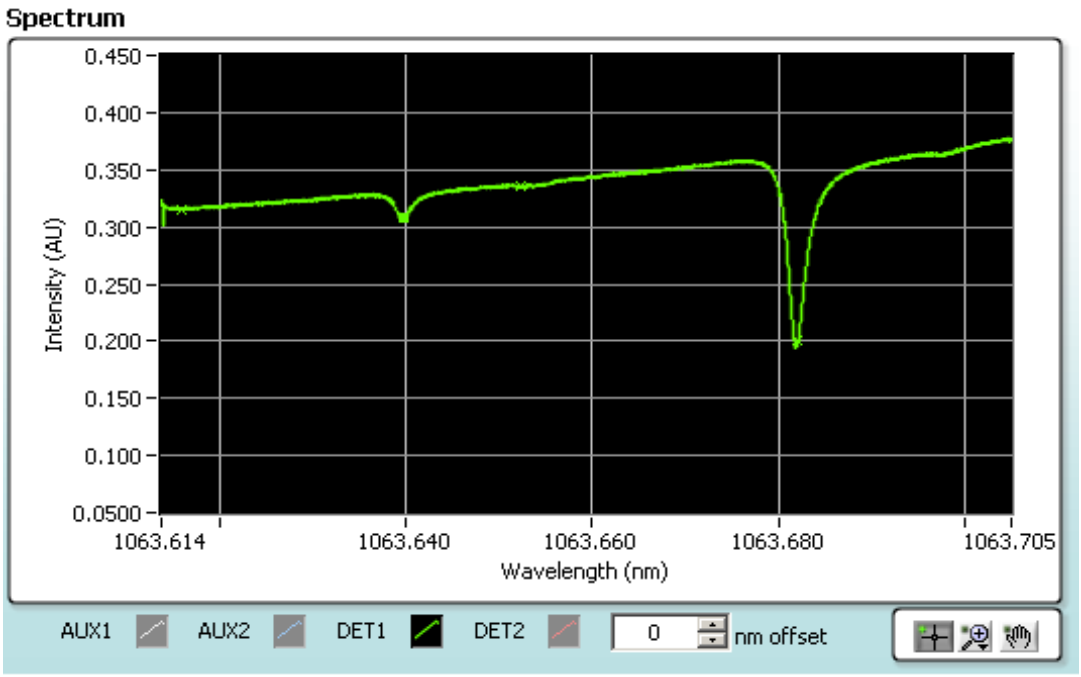

Figure 30: Mark-I GUI of the TE spectrum. Small, shallow dip represents the *m = l* resonance and the larger, steeper dip is the *m = l-1* resonance.

The dips from left to right represent the *m = l* and *l-1* modes respectively. As can be observed, the *l* mode dip is much smaller and shallower compared to the *l-1* mode dip; this

is a qualitative measure of coupling strength to each mode. In this case the fiber is touching the resonator at the equatorial latitude and thereby interacts with all fields specified by the spherical harmonic function to have a peak there (even q numbers, where $q = m\text{-}l$). The interaction dampens the resonance at those locations and leaves all modes with odd q values relatively unperturbed. The goal here was to under-power one mode compared to another mode so that one mode serves as a 'preferred' optical trap. Meanwhile, the other mode serves as a real-time monitor to help analyze latitude of the bound particle.

What was observed over the course of the experiment was that the power going into either mode was much too low to form a strong enough optical trap in order to capture particles at the surface. What was seen, instead, were repeated 'carousel' events characterized by momentary wavelength shifts corresponding to particles drawn into the modal volume and then a return to the original wavelength indicating that the particle escaped orbit.

As was shown in the theory section, it is possible to promote binding by increasing the salt concentration, however, this decreases the Debye length over the whole sphere. The result would be non-specific binding and would not demonstrate light force assisted trapping. Another idea could be to increase the power delivered through the fiber into the sphere. This, however, proves difficult as much of the light is lost from the laser source due to insertion losses from in-line components, scattering losses from the taper of the waveguide, coupling losses and the scattering due to the curvature of the resonator. Furthermore, there are hardware limitations on the Mark-I which do not allow for more power to be injected than what was used.

However, the reader may re-call that energy is defined by power multiplied by time. The average energy going into the above system is characterized by how long the laser spends on each dip and therefore if the time spent per dip could be increased then the average energy delivered to each mode is increased without actually increasing the power in the incident light source. The solution was arrived by 'skipping' wavelengths:

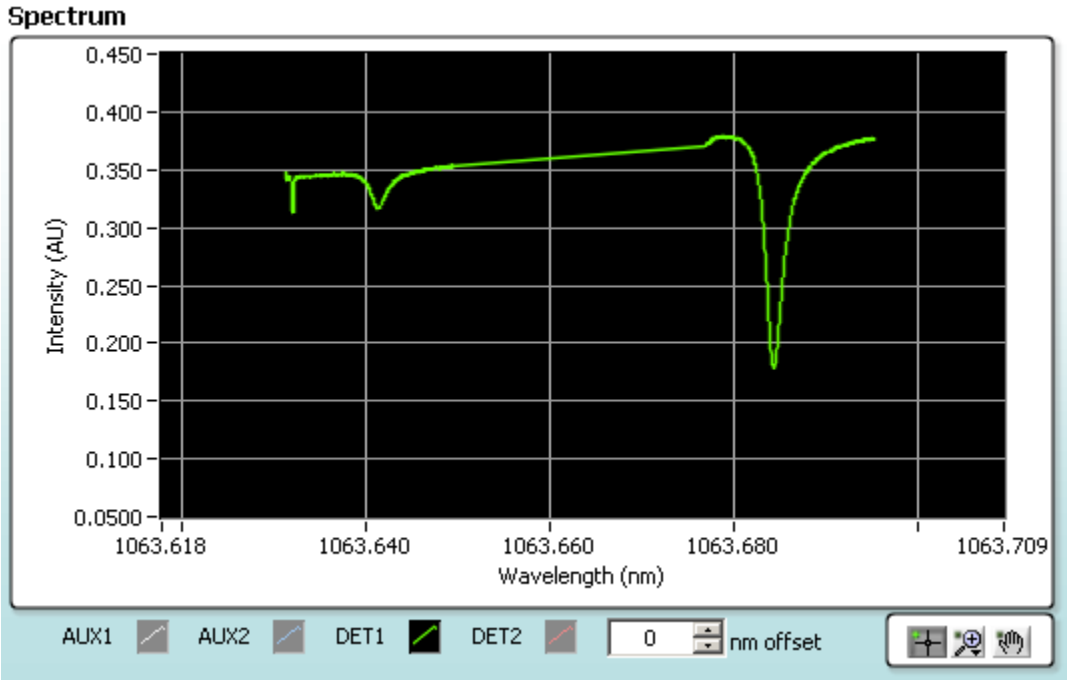

Figure 31: Compared to Figure 25, Mark-I GUI of a skipped laser spectrum including the *l* and *l-1* modes (from left to right)

Here the first dip is scanned until a wavelength of about 1063.650 nm after which the laser jumps (seen by the slender 'connecting' line in between two dips) to a wavelength of about 1063.678 nm. The average energy of this spectrum is calculated to be about 2.5 times that of the spectrum pictured in Fig. 30.

The reader may notice that the spectrum has an additional feature on the left and is slightly red-shifted compared to the previous spectrum. Both are, indeed, due to the new

scanning scheme. They are the result of laser hysteresis. At lower wavelengths the laser starts at a lower current and as higher currents are fed in the laser is driven to higher wavelengths. At the end of the scan the laser must return to its original wavelength, and it snaps back as fast as possible. However, lasers cannot truly 'skip' wavelengths and so the hysteretic dip is the result of a speedy backward scan de-limited by the thermal relaxation time of the laser. Fig. 30 also shows this hysteretic dip if it is observed closely but is noticeably smaller and shorter; in this case the laser has to 'snap back' more often per time period and thus maintains a slightly higher temperature which red-shifts the spectrum.

The current fed to the laser can be visualized for both Fig. 30 and 31:

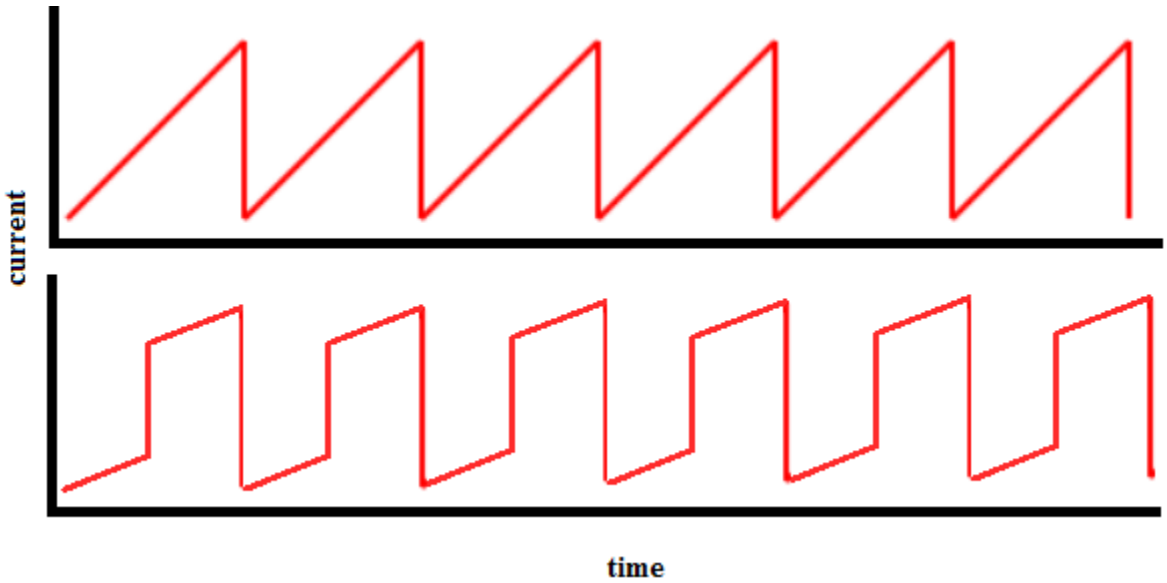

Figure 32: A sawtooth function for current was fed to the laser. The top profile represents the scanning scheme used in Figure 30 and the bottom is the scanning scheme used in Figure 31.

As DFB lasers generally have linear light-current (L-I) curves, the power output displays would most likely hold a similar profile, however, the sharp dips in current would look closer to sharply decaying exponential curves with a decay time characterized by the thermal relaxation time specific to the laser system at hand. As is observed, wavelengths are not actually skipped as they are related to the current input of the laser, instead, the

‘wavelength skip’ scan is produced simply by ramping more slowly over a given scan range and then suddenly providing more current to ‘jump’ up to the next wavelength.

B. LFA RESULTS

The exact experiment pictured above actually did not have enough power to attract particles to the surface even after the ‘wavelength skip’ scan was utilized. As it turned out the system was limited by ‘over coupling’ to the system; a scenario where a fiber that is not pulled taught onto the face of the glass slide sags under the weight of the resonator and instead of maintaining single point contact, wraps around the resonator coupling over a large length which leads to large scattering losses from the sphere reducing the amount of baseline power that the system receives and can subsequently use for trapping.

Fortunately a repeat experiment done in the same manner did not have this problem and from $m = l$ and $l\text{-}1$ shifts, a binding location and radius was successfully determined for 9 events:

Event	$\Delta\lambda_{m=l}$ (fm)	$\Delta\lambda_{m=l-1}$ (fm)	ξ (°)	$r_{experimental}$ (nm)	$r_{manufacturer}$ (nm)
1	453 ± 10.0	515 ± 10.0	2.36 ± 0.900	226 ± 13.0	228 ± 7
2	92 ± 10.0	414 ± 10.0	4.67 ± 0.900	236 ± 13.0	228 ± 7
3	259 ± 10.0	513 ± 10.0	3.09 ± 0.900	212 ± 13.0	228 ± 7
4	677 ± 10.0	314 ± 10.0	1.50 ± 0.900	233 ± 13.0	228 ± 7
5	225 ± 10.0	552 ± 10.0	3.45 ± 0.900	222 ± 13.0	228 ± 7
6	276 ± 10.0	571 ± 10.0	3.11 ± 0.900	219 ± 13.0	228 ± 7
7	582 ± 10.0	548 ± 10.0	2.14 ± 0.900	243 ± 13.0	228 ± 7
8	348 ± 10.0	263 ± 10.0	2.52 ± 0.900	207 ± 13.0	228 ± 7
9	445 ± 10.0	480 ± 10.0	2.97 ± 0.900	206 ± 13.0	228 ± 7
MEAN	**373**	**463**	**2.87**	**222**	**228**

Table 1: Analysis of 9 binding events of PS particles having a manufacturer specified ensemble average radius of 228 nm. Wavelength shift data is used to find both latitude and radius.

From the data it is observable that the wavelength shifts translate to calculated radii quite close to the manufacturer suggested numbers, with the mean deviating only about 2.6%. Much of this deviation can be accounted for by error bar overlap; had manufacturer tolerances been tighter then stricter sizes could also have been expected. Here we see a histogram representation of the calculated radii with a Gaussian distribution of the manufacturer's radius shown:

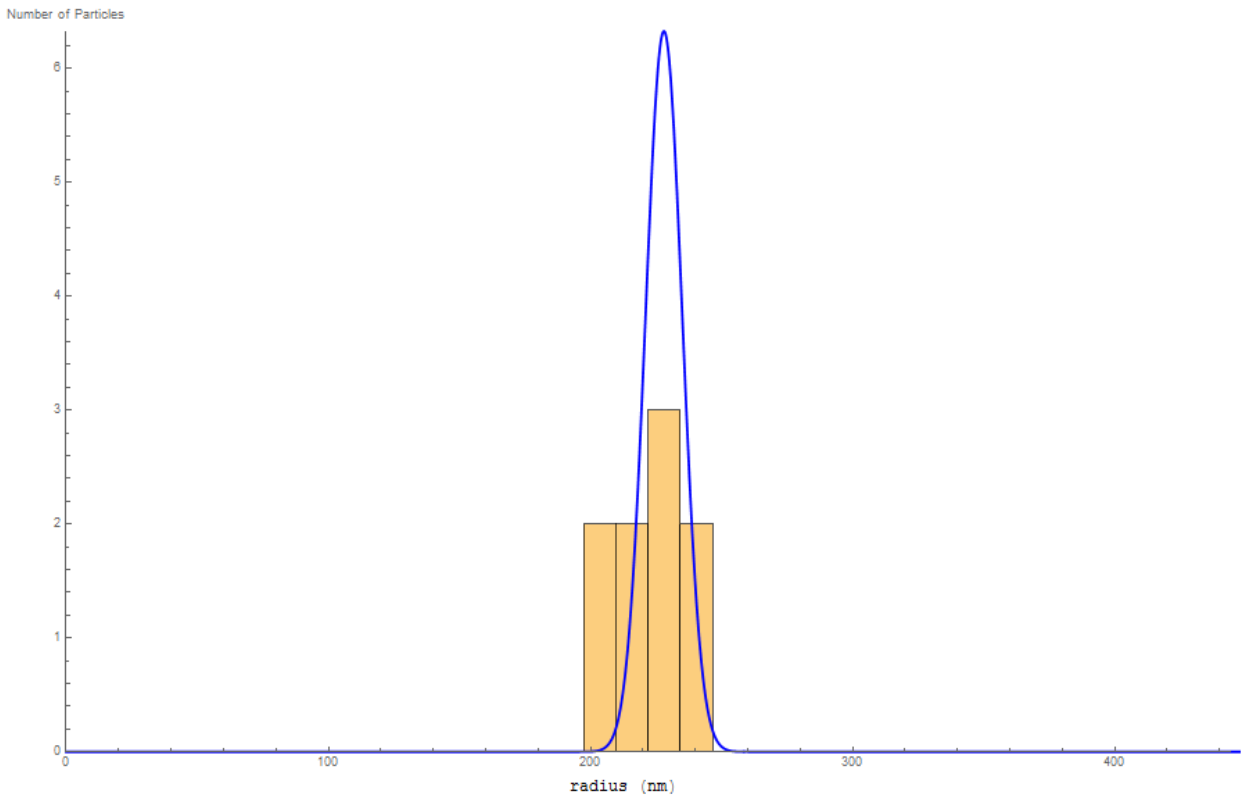

Figure 33: histogram data of radius distribution of PS particles with an overlayed gaussian distribution constructed from the manufacturer given mean and tolerance with equivalent area under the curve to the histogram

As the experimental radii match with good accuracy to expected values, we may take this to be an implicit check that experimental error and artifact were minimized.

A range of latitudes are seen and can be overlapped with a potential plot of Y_l^{l-1}:

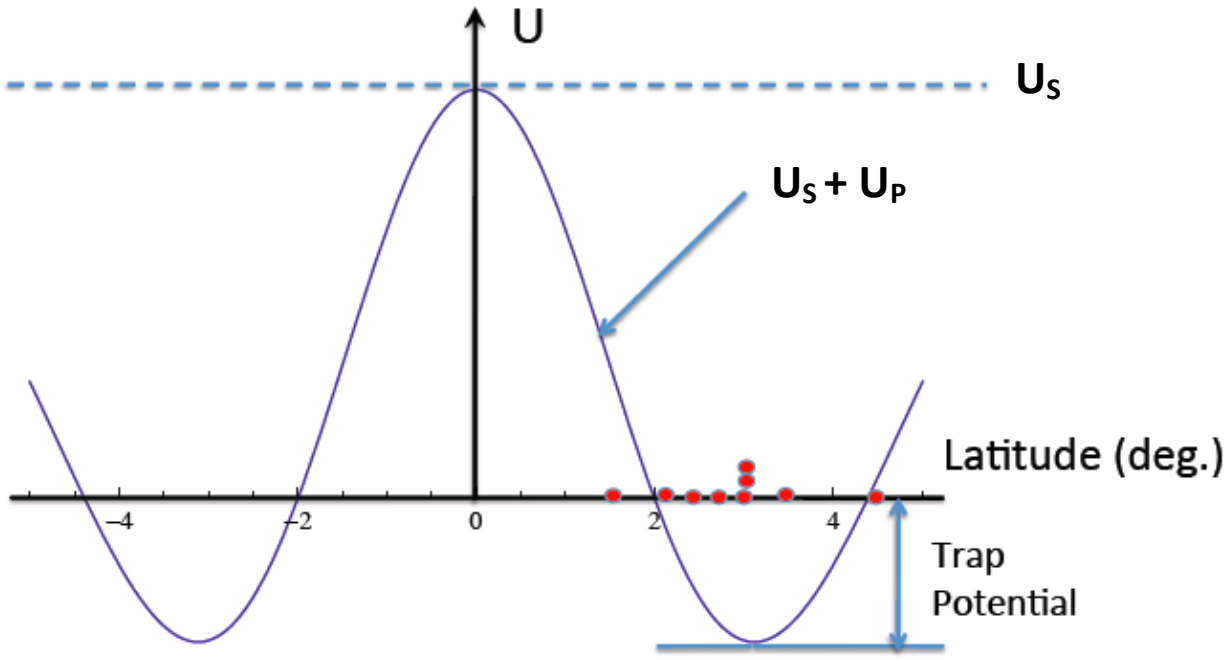

Figure 34: Potential plot with optical potential for m= l-1 modes overlayed with latitude data represented as red dots from particle binding events. Potential values are arbitrarily picked to demonstrate trapping due to optical potential.

Here the x-axis represent latitude in degree, the y-axis corresponds to values of the potential, U, each red dot approximates the locations of particle binding events from Table 1. The peak of the curve represents a 0 contribution from optical potential, U_p, thus leaving only the electrostatic Debye potential at some positive value. As one moves closer toward the valleys, it is clear that the optical potential works to counter the Debye potential and reaches a negative sum potential at some latitude. The lower the value of the potential the more particle bindings one can expect in such a location and so the graph above is

constructed in a manner attempts to show such an effect. Qualitatively we are able to see a clear correlation between the location of the particle binding events and the *l-1* mode.

However, since we do not exactly know the value of the potential as a function of latitude (at least not fully, more work has to be done before this is possible), we can simply compare the mean binding location of the particles with the minimum of the potential. The mean, as is shown in Table 1, is 2.87° and the minimum of the potential curve occurs at roughly 3.11°; well within one standard deviation.

Thus there is good preliminary evidence of the principle of LFA. So far the theory seems self-consistent with the experimental outcome. Additionally, multiplying the standard deviation by the radius of the sphere (~41,500nm) we can calculate the arc distance within which we are able to space each particle to be around 650nm, which gives credence to calling this a nano-fabrication technique.

For the completion of this project data has to be repeated for the *m=l* mode, as well, in order to ensure that the effect wasn't biased by experimental circumstance. For example, one phenomenon that is often noticed is of the particles traveling along the length of the waveguide fiber (which carries its own evanescent field) quite readily. Naturally as it follows this trajectory the particle is favorably dropped off near one of two sensing regions and was never in a Brownian walk thus introducing a possibly artificially enhanced preference for particular regions.

V. BARIUM TITANATE RESONATORS

Silica has long been a mainstay material in optics and subsequently enjoyed large-scale commercialization by the telecom industry. However, as discussed before, improving current detection limits is one of the sensing requirements for analysis of bio-complex systems and generally is simply a forward-looking step toward other real-world applications. There are many high refractive index materials that have been explored in the application of whispering gallery mode resonators, including polystyrene, titanium dioxide and even barium titanate (BT). Due to its exceptionally high refractive index BT has been chosen as a candidate in this thesis toward improving sensitivity.

A. INCREASING WAVELENGTH SHIFT BY DECREASING RADIUS

In this thesis project, decreasing the bare micro-spheroid's size from a radius of 40μm to a radius of 10μm was chosen as the primary mode of increasing wavelength shift per particle. From chapter 2 Eq. 25 can show us, all other morphological features kept the same, the magnitude of expected sensitivity increase. For an analyte binding event at latitude, ξ_p, of size g(z) we have an increase of roughly (but not exactly due to evanescent field corrections):

$$\frac{\Delta\lambda_{R=10\mu m}}{\Delta\lambda_{R=40\mu m}} \approx \frac{(40\mu m)^3}{(10\mu m)^3} = 64 \qquad \textbf{Eq. 36}$$

On top of increasing the sensitivity of a binding event a reduced radius indirectly supports requirement (4) by reducing the total amount of surface area for interactions of non-interest to occur and allows for sensing over a tighter volume reducing the amount of background noise.

B. REFRACTIVE INDEX CONTRAST

Material limits are one of the factors that restrain the decrease in size of silica cavities. As was shown by S. Arnold *et al.*[43] in the figure below, at a wavelength of 780nm, 40μm is the size limit of silica after which the floor of detection is raised.

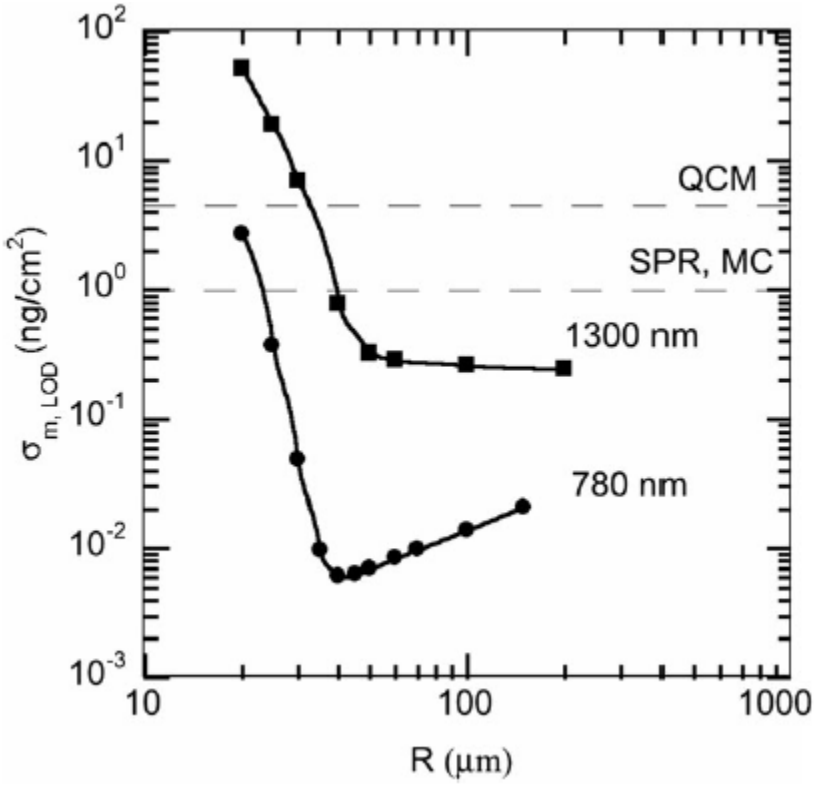

Figure 35: Smallest theoretical detectable uniform mass per surface area of a silica cavity submerged in water as a function of radius for two different wavelengths. The assumed smallest shift was 1/50th the linewidth and ξ_p assumed to be on the equator. QCM, SPR and MC denote the limits of detection of Quartz Crystal Microbalance, Surface Plasmon Resonance and Micro-Cantilevers.

As is detailed by the paper, the Q-factor of a mode degenerates roughly with the intrinsic losses (due to tunneling) and absorptive losses (due to the surrounding medium or by the cavity material):

$$\frac{1}{Q} \approx \frac{1}{Q_{intrinsic}} + \frac{1}{Q_{absorptive}} \quad \textbf{Eq. 37}$$

The absorptive processes can be seen in the difference of limit of detection (LOD) between the 780nm and 1300nm lasers; the surrounding medium was assumed to be water which has a roughly linear absorption curve between 400nm and 2000nm, with the peak being at 2000nm.

The intrinsic losses include material losses and radiative leakage due to curvature[44]. As was described before, the light is confined temporarily via *almost*-total internal reflection. TIR is only allowed at a certain incidence angle called the 'critical angle' which occurs on flat plane surfaces, which can be thought of as spherical surfaces with infinite radii. As the radius is decreased, the curvature (defined as 1/R) increases and the deviation away from the critical angle increases; thereby leading to light leaking out. For silica these losses tend to dominate around a wavelength to diameter ratio of 50.[45]

The losses due to radius reduction can be counter-acted by a decrease in material losses. As described by Ilchenko *et al.*:

$$Q_{material} = \frac{2\pi n_s}{\alpha\lambda} \qquad \textbf{Eq. 28}$$

where α is the absorption coefficient of the material. As can be seen, a higher refractive index allows a greater $Q_{material}$ ceiling and a lower absorption coefficient. Though literature data on barium titanate glass absorption coefficient is not readily available to show a sample calculation of $Q_{material}$ comparisons for the two materials in question, chapter 2 might be recalled to see that the BT has a refractive index of around 1.95 (compared to fused silica's, 1.47) which works to reduce tunneling losses due to high curvature by way of smaller cavity radii, allowing for a higher sensitivity.

C. COUPLED BARIUM TITANATE RESONATOR ASSEMBLY

Unlike previous experiments where the silica resonator was attached to a post and could be maneuvered into position atop the waveguide fiber, commercially ordered BT particles had no such convenience as telecom-grade BT optical fibers were not available.

A few particular approaches were attempted to achieve a sphere-waveguide construct. The first hurdle was to find a way to 'pick-up' the BT spheres so as to be able to manipulate them. The inspiration for the first method tried came from previous work done within the lab[46] that had successfully delivered polystyrene spheroids that were 41 μm in diameter. This involved using a micropipette to deposit 10 μL of an arbitrarily dilute mixture of BT in DI water onto the tip of a clean tapered fiber.

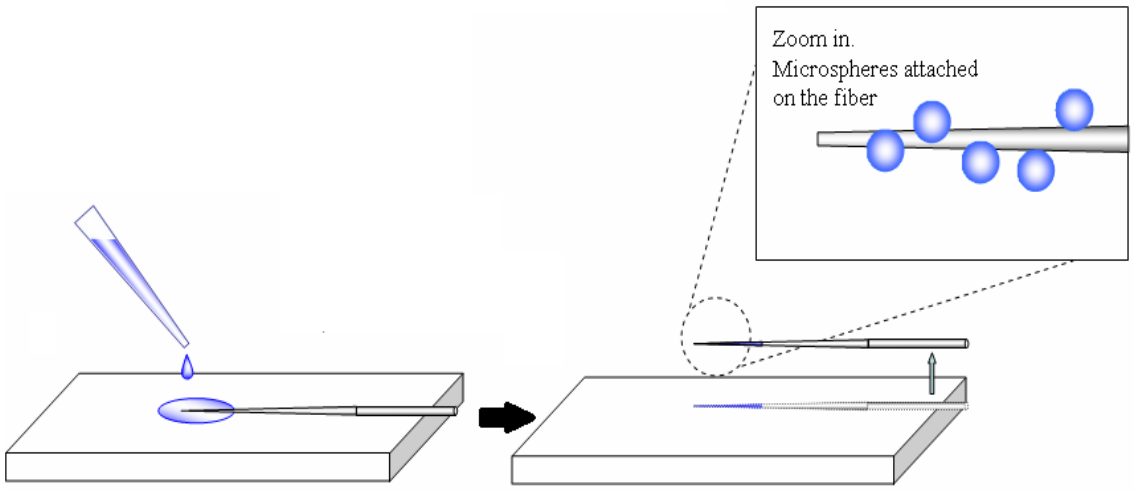

Figure 36: Process of attaching free BT spheroids onto the end of a tapered fiber

The ‘delivery’ fiber was then picked up and put on the XYZ stage in order to place the BT on the waveguide; the goal was to have van der Waals forces associate the BT spheroids to the fiber. What was quickly learned was that after being picked up off of the acrylic sheet BT would, only rarely, be present on the delivery fiber and when they were it was generally on the thicker portion of the fiber tip (empirically measured to be around 40-50μm taper diameter).

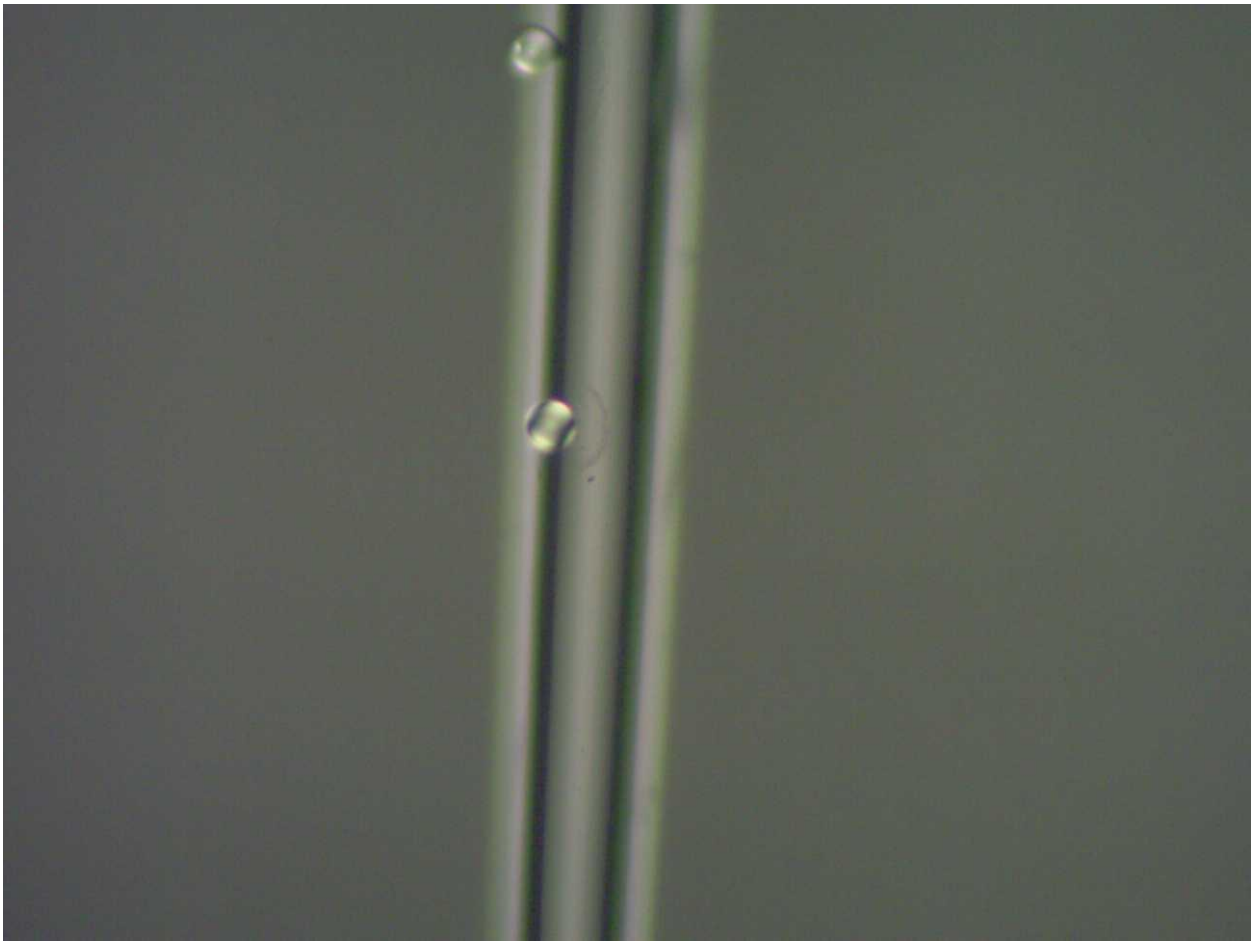

Figure 37: BT spheres affixed to a tapered silica fiber near the 40-50 μm taper diameter region.

In lieu of this, it was clear that the low odds of success demanded a procedure that allowed for more trials in a shorter period of time. A modification to the method was made in an attempt to facilitate this. What was discovered was that the BT-fiber association was not strong enough to overcome passing through the water-air interface whilst being picked up off of the acrylic sheet and on to the XYZ stage. Instead a BT in ethanol mixture was used for subsequent experiments with the idea that ethanol evaporates relatively quickly, so it was not necessary to pull the BT-decorated fiber through a water-air meniscus. It turns out that the cavity-fiber assembly was able to hold together during ethanol evaporation

(which may be due to a lower surface tension for ethanol-air interfaces compared to water) and had a greater success rate than picking up the fiber out of water, with a success rate of about 1 in 3 attempts due to other problems such as loss of BT particles while physically transporting the delivery fiber from the acrylic sheet to the microscope stage.

Next a transfer from the delivery fiber to waveguide fibers was attempted in air by a 'rubbing' motion in order to coax the BT spheroids off of the delivery fiber via mechanical stress. Generally this was a difficult task, either it was impossible to 'unstick' them from the delivery fiber or they would simply fall off of the delivery fiber without 'sticking' to the waveguide fiber. As a result, a success rate of about 1 in every 15 attempts was achieved, which, as is discussed later is not a viable option (for reasons other than having to spend an exorbitant amount of time).

The reason this method might have worked with polystyrene and not with BT could be due to the large difference in size and density. The density of BT is approximately four times as large as that of polystyrene which means that a greater attraction force per interacting dipole was necessary in order to keep it preferentially associated to a silica fiber. Since the BT particles were about 8 times less voluminous than the polystyrene particles less dipoles are close enough to the BT-silica interface that can be recruited to take part in the interaction. We might then infer that in order to associate with silica the BT would prefer greater taper diameters where more dipoles are in range due to reduced curvature which would then increase the interaction area and thus total force that holds the BT in place. Unfortunately, since the waveguide fiber is made of the same material as the delivery fiber but has a smaller tapered diameter of just approx. 2-5 μm, there is little incentive for BT particles to transfer, even after the use of mechanical force (rubbing motion).

The interaction dynamics had to be changed due to these issues. One option was to consider using a different material post as a delivery agent. However a tapered fiber, due to its narrow diameter, was the most convenient option for precise delivery and was not easily replaced by another material of different properties (in the hopes that the transfer could be eased). Lifshitz theory[47] mentions that the interaction medium changes interaction dynamics. Thus different media were tried as a 'pick-up' medium including DI water, 30mM NaCl solution, methanol, ethanol, n-propanol, iso-propanol, hexane, toluene, acetonitrile, and acetone. The goal was, ideally, to be able to pick up BT in a medium that did not promote overly strong BT interactions with the delivery fiber. Additionally the 'picking-up' process was, now instead of on an acrylic sheet, done directly on the slide which already had the waveguide fiber on it in a region away from the BT pick up location, with the added benefit that a microscope could now be used to monitor how the BT interacted with the fibers during pick up as well as subsequent transfer to the waveguide fiber.

What was found was that many of these media promoted BT aggregation including DI water, hexane, and acetonitrile. In order to resolve this issue, an even more dilute concentration of BT-media mixture was used, with a qualitative target concentration aiming to observe only a sparse BT mono-layer on the slide surface. Of the media that did not promote strong BT aggregation (IPA, DI water with NaCl, n-propyl alcohol, acetone) it was found that the BT and silica surface of the microscope slide had a strong interaction. As a result the 'picking-up' process would become difficult due to the delivery fiber 'sling-shotting'. The lowered fiber would cling to a BT particle and as the XYZ stage would be moved up in the Z direction so as to raise the fiber up, the fiber tip would remain stuck

while the rest of the fiber would bend until the bending threshold would overcome the interaction of the fiber tip and the BT particle after which it would ‘sling-shot’ up and scatter all particles in the vicinity.

Therefore, instead of using a tapered delivery fiber, silica spheroids (made by the CO_2 laser, of ~100 μm diameter) were used instead as the pick-up and delivery agent. While not completely ‘sling-shot’ free it had better success than the tapered fiber. It also changed the geometry of the interaction by nature of being spherical instead of cylindrical. What was observed was a greater success rate in being able to pick up BT spheroids and a greater rate of dissociation from the BT spheroid when a transfer was attempted.

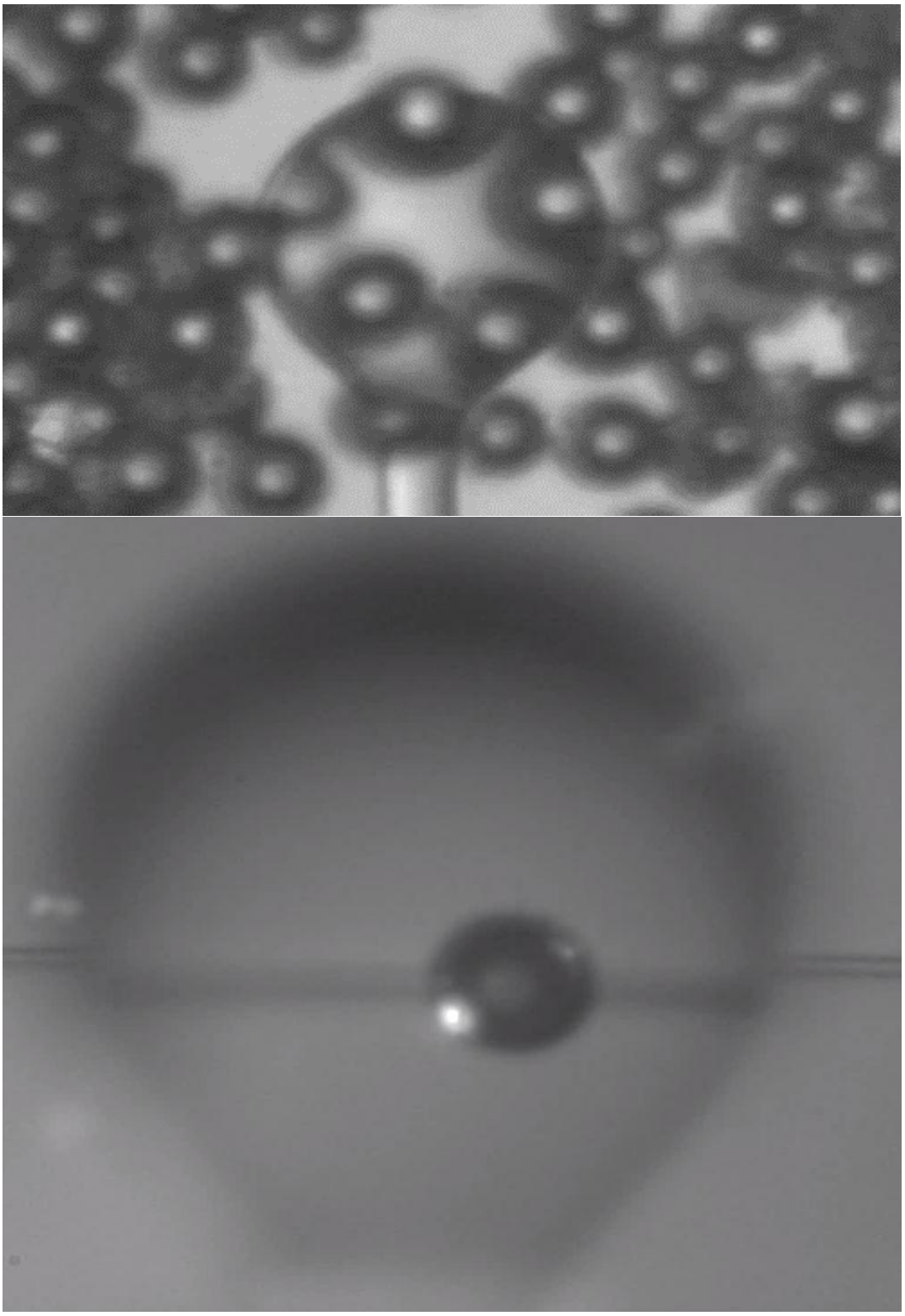

Figure 38: Top: silica resonator being driven through a pile of BT spheres. Bottom: Silica sphere with a single BT sphere adsorbed being brought in proximity to the waveguide.

In the end, the use of the silica spheroid as a delivery agent eased the process greatly and even allowed the transfer to occur while the waveguide fiber and BT spheroids were completely immersed in water. Other media exhibited a variety of different effects on the overall process but none that greatly improved the success rate of that over water. It was noted that a transfer done in air was generally more difficult than one done within liquid (thereby eliminating all quickly evaporating media), and that 'picking-up' was much easier in a 30mM NaCl in DI water solution but that transfer was impossible given that the BT particles displayed almost no interaction with the waveguide fiber (after 'rubbing off' the particle would simply fall off the waveguide fiber).

D. RESULTS

After all of the modifications done to the delivery procedure the success rate of getting a BT sphere onto the waveguide fiber went up to about a 1 in 2 trials (each consisting of about 10-15 minutes). As discussed earlier, time spent during the delivery process was not the only barrier to successfully seeing resonances. Due to the size and refractive index of BT the chances of seeing resonances were quite different from that of standard sized, laser heat-formed silica spheres. The size and refractive index of the resonator affect the separation between continuous *l* modes; called the free spectral range (FSR). That is, assuming for a moment that the resonator is perfectly spherical, we know from Eq. 1 that a different number of wavelengths will fit within a given circumferential path for different wavelengths. Due to the use of a 1064nm DFB laser, we may calculate the number of wavelengths of TE polarized light at 1063nm in orbit around a BT resonator roughly 20 μm in diameter with refractive index of ~1.95 via Mie theory provided in

chapter 2, $l \approx 107$ with a corresponding optical size of $X_{TE,107} = 59.0276$. The FSR can be given by calculating X_{TE} at *l-1* ($X_{TE,106} = 58.5008$) noting the change in wavelength from one *l* to the next:

$$FSR = \lambda_l - \lambda_{l-1} = 2\pi R\left(\frac{1}{X_{TE,l}} - \frac{1}{X_{TE,l-1}}\right) = 9.58\ nm \qquad \textbf{Eq. 39}$$

Unfortunately the scan window of the DFB laser only spans a maximum of about 3nm bringing the chance of seeing a resonance for any given trial to 1 in 3.

Needless to say, after a few deliveries resonance was seen:

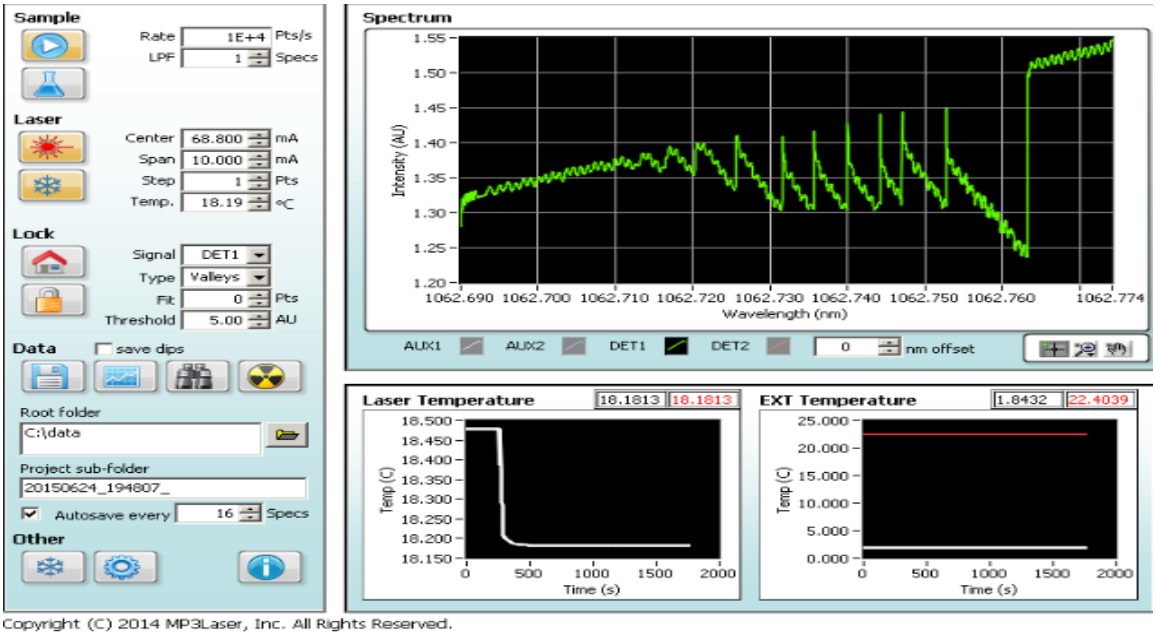

Figure 39: Mark-I GUI showing spectral scan at high power

There may be doubt as to whether what is seen above is a true resonance as it does not hold a Lorentzian shape, however, it was noted during the experiment that a total of 1.5mW of power was being delivered through the fiber and non-linearity in behavior might be explained by the high intensity of the driving laser.

Optical bi-stability is one possible explanation. That is, due to the high intensity delivered to the sphere, an even higher intensity build-up might occur within the resonator causing the resonator to heat up and expand at resonance. As Eq. 1 shows, the larger the radius of the resonator the larger the wavelength of light required to travel along the inside. It is possible to suggest then, that once resonance is reached the sphere starts heating and expanding and as the laser scans to higher wavelengths it chases this required wavelength for a while until the expansion of the sphere can no longer keep pace with the scanning rate of the laser and a sudden 'snap-out' of resonance is seen and the intensity jumps back up and out of resonance. Another possible explanation might be by way of the Kerr effect. The heating of the sphere causes a shift in the refractive index which, if shifted to higher indices, would also cause the required wavelength to increase. Unfortunately it was not possible to determine the contribution of thermal expansion and the thermo-optic coefficient (changing *n* with temperature) due to insufficient literature data for amorphous BT.

As may be suspected, lowering the intensity of incident light produced Lorentzian type dips:

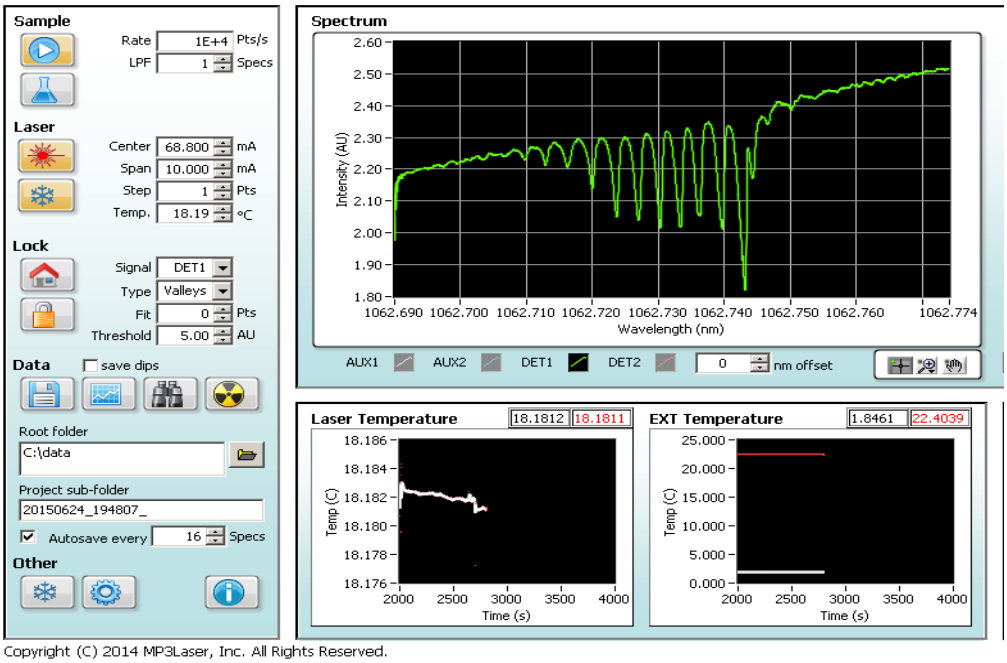

Figure 40: Mark-I GUI showing spectral scan at low power

The estimated power of the incident light was measured to be about 20-30 μW. In an attempt to get qualitative confirmation that it was indeed a resonance being seen, the stage Peltier heating block was heated from 23°C to 31°C. As expected a shift in resonance occurred due to varying contributions from thermal expansion and the thermo-optic effect as explained earlier:

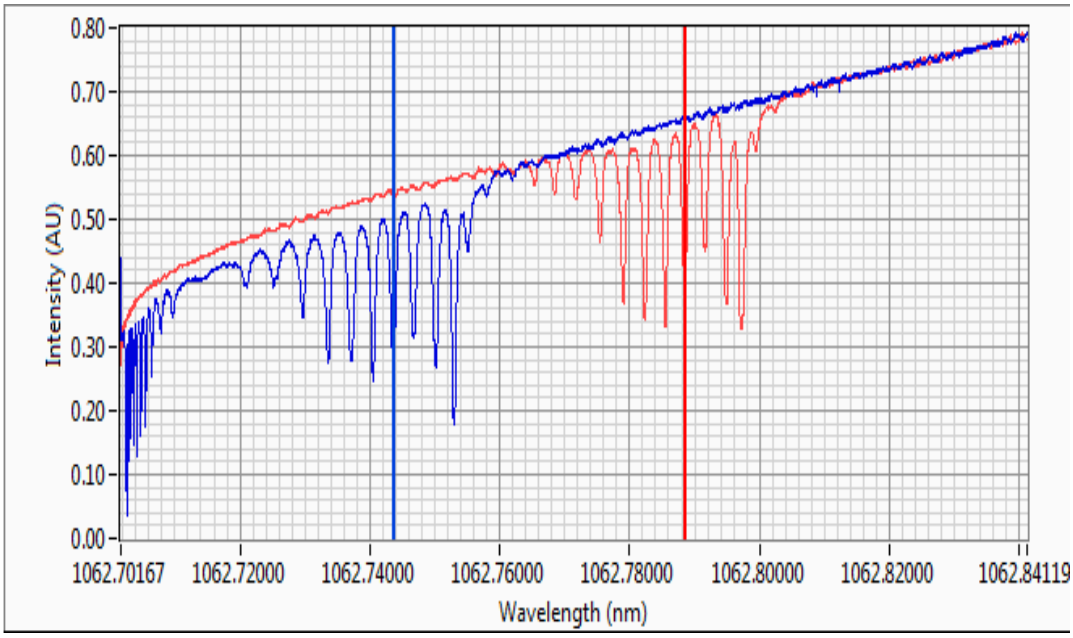

Figure 41: Blue is resonance at 23°C, the red is resonance at 31°C

The Q-factor for some of the dips observed reached 1E+06! This can be compared to previous experiments done by Astratov *et al.*[48] where coupling BT spheres of diameter 14 μm yielded a Q-factor high of about 3 E+04. Below is a sample of their findings:

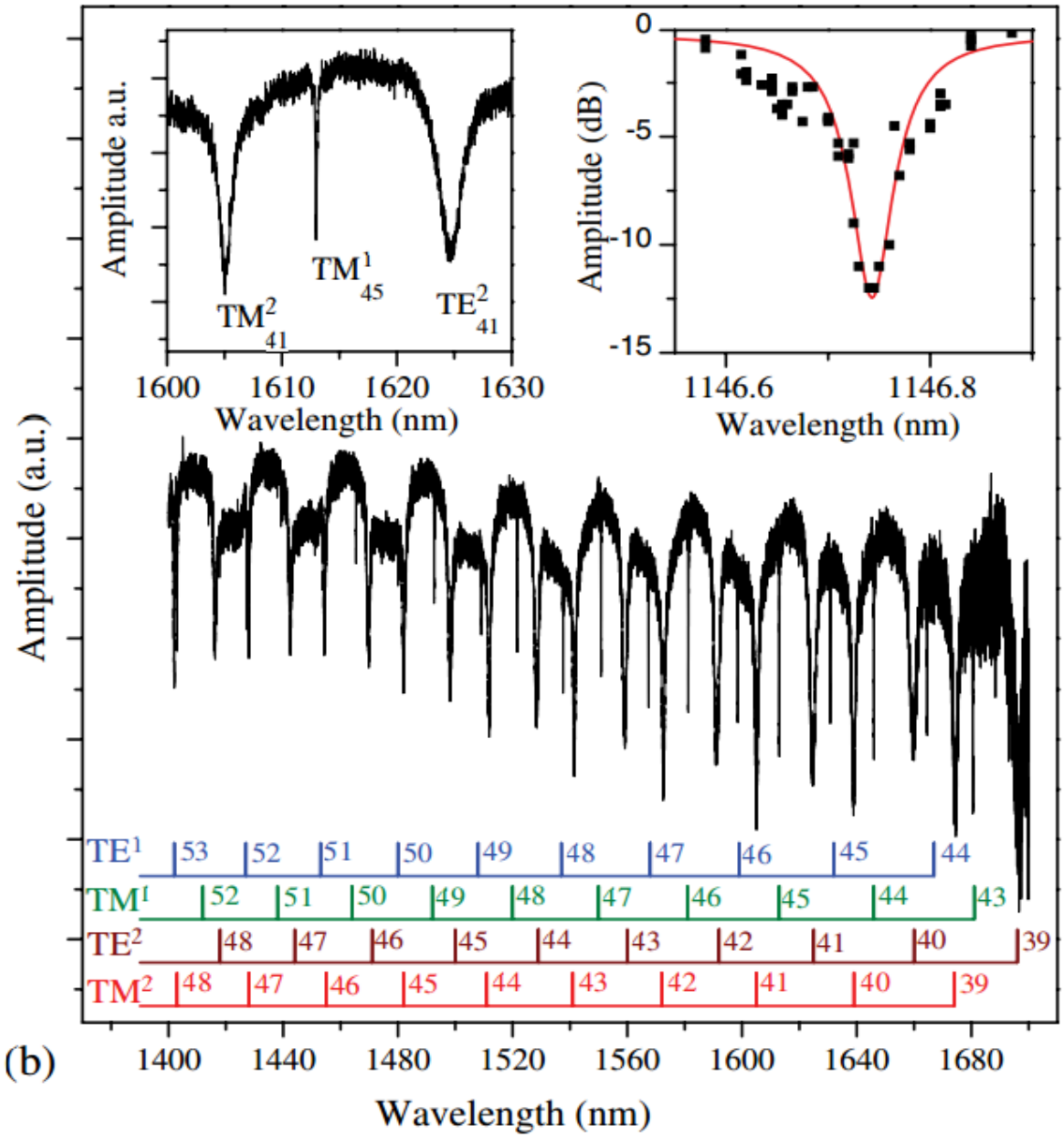

Figure 42: Bottom diagram marks calculated resonances. Left resonance shows enlarged portion of the spectrum. The right spectrum is one of the resonances.[48]

It is most likely that the ~33 fold increase in Q was a result of a combination of different factors. Lower wavelengths were used in our experiments (which, the reader may recall,

absorbs less in an aqueous environment), slightly larger spheres (which may reduce curvature related losses), different sphere morphology (Although both were ‘BT’ spheres, this is technically not enough to consider them equivalent materials. A large difference can come from the proportion of Barium to Titanate in each glass which is a function of how they were mixed. Other differences might include eccentricity to different lasers (DFB vs. semiconductor laser). It is unlikely that any real difference was caused by laser resolution in the two experiments; both lasers have extremely narrow resolution that exceed the achieved linewidths. A drawback of the DFB laser however can be demonstrated by the presence of both TE and TM modes in Fig. 42. The data presented in this thesis only contained TE modes which were observed during the experiment by changing the polarizer. According to the left insert in Figure 19, for the same l number, TE and TM mode separation is over 10 nm and is clearly not observable within the DFB’s narrow scan window. As was carried out in chapter 2, a quick calculation for the expected shift of the resonators used in this experiment of a TM mode relative to the TE position yields 9.72 nm; agreeing with the aforementioned results.

Another question that may be asked is if Astratov *et al.* report broadening of observed dips due to *m* mode overlap; then it is interesting to wonder why it is that a single dip in both sets of data look Lorentzian. This is demonstrated intuitively by observing an increase of linewidth off all dips by 33x in a set of simulated Lorentzians normalized for area:

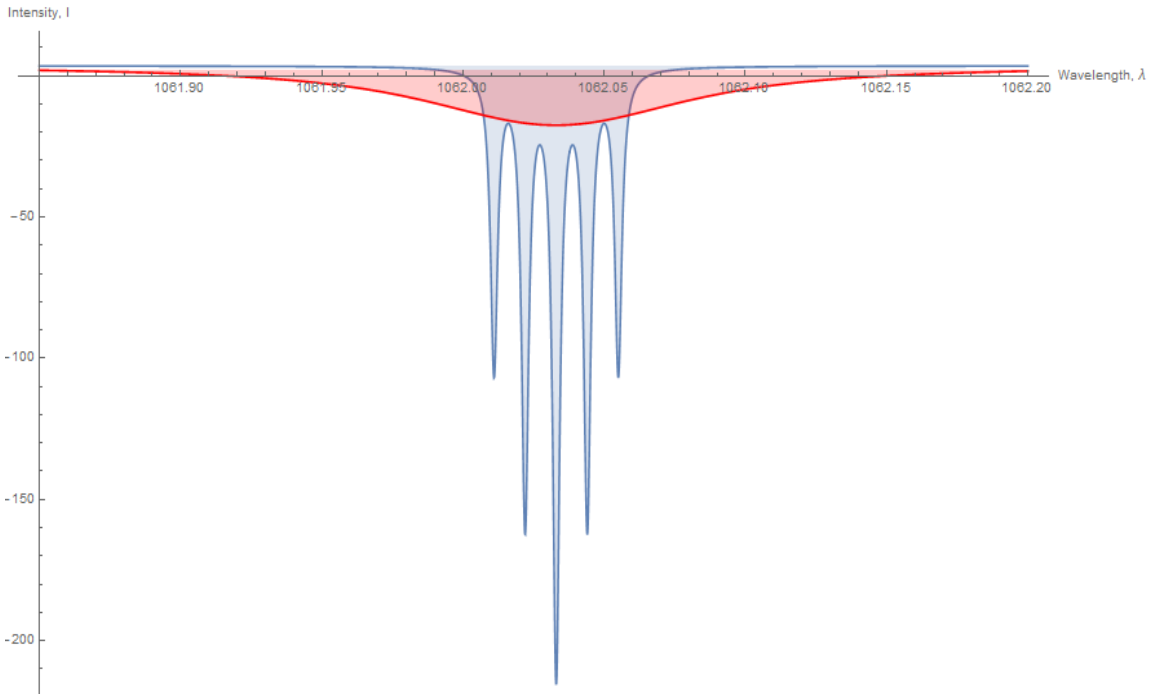

Figure 43: Blue: Set of simulated Lorentzians with a linewidth, Γ = 0.003. Red: Same set of Lorentzians with linewidth 33x higher.

Although the broadening looks extremely flat, this is because both sets of Lorentzians are normalized to have the same area. If we expand the red we reveal:

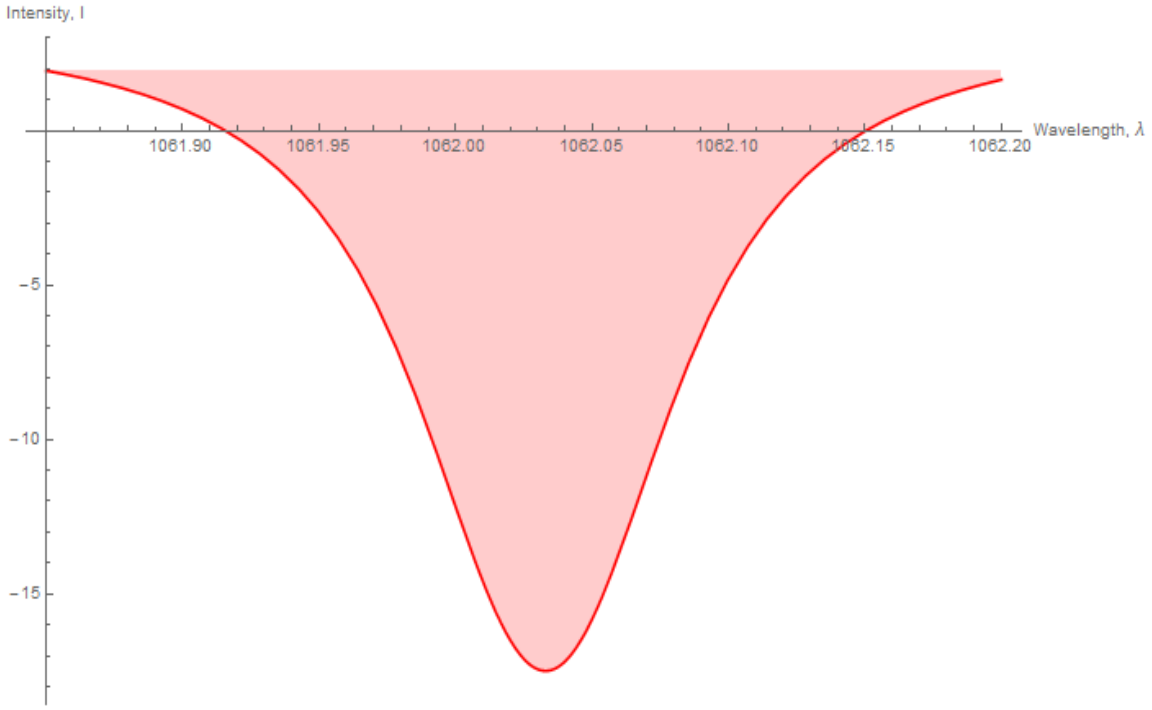

Figure 44: Blown up version of Lorentzian curves in Figure 43.

Qualitatively the resultant graph looks roughly Lorentzian and therefore asserts the hypothesis that what we are seeing is not a different feature but simply sub-structures of what was seen earlier. It is also important to note that, in case, any differences in spectra observed between the two groups are contributed from, not only physical phenomena as discussed, but be the result of hardware induced resolution differences then instead of adding Lorentzians together via linewidth broadening one convolves them. Indeed the convolution of two Lorentzians yield a Lorentzian.[49]

E. SMALLEST THEORETICALLY DETECTABLE SHIFT

Although no actually experiments have been committed toward finding the smallest particle that can be sensed we are able to make some assumptions and arrive at an estimate. The first step is to find the characteristic length of the evanescent field, L_E, via Mie theory. Taking refractive index of the cavity, n_s = 1.95 and that of water, n_e = 1.326 at an approximate wavelength of λ = 1063nm an angular momentum number, l = 107 satisfies the radius requirement of a 10 μm resonator (approximately, R = 9.9864 μm).

The evanescent field is then taken to be the length at which the field intensity at the boundary falls to 1/*e* of its original value. If R = 9.9864 and the field there is 79.0356 (in arbitrary units, AU). Then the value 79.0356/*e* demarks the intensity at $R_{1/e}$ = 10.06 μm:

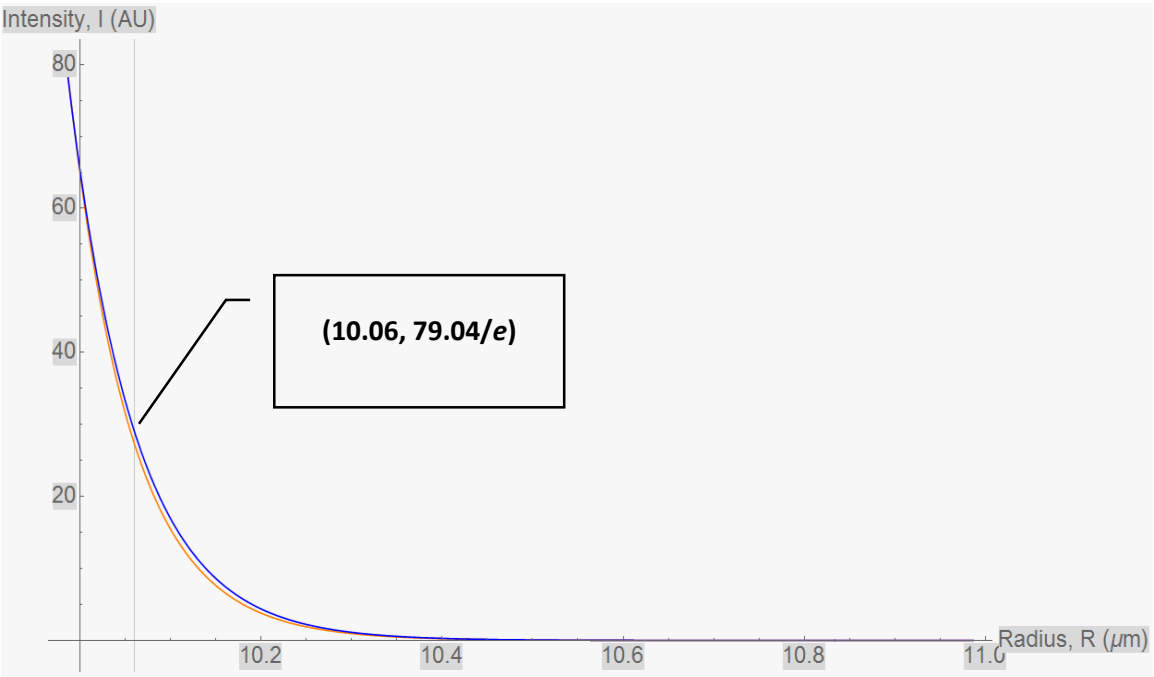

Figure 45: Evanescent Field Intensity outside of the sphere. Orange: Hankel function Blue: exponential approximation. Gray vertical line demarks $R_{1/e}$ = 10.06 μm.

The exponential fit is given in blue for reference for the reader to show that it is not so far off for a fit from, R to $_{R1/e}$, to the Mie theory derived Hankel function. Thus the evanescent length, L_E = (10.06 – 9.986) μm = 73.6 nm.

Now we re-call from Chapter 2, equation 23, 28 and 29, which express size of the analyte in the form:

$$a^3 g(z) \approx \frac{(n_s^2 - n_e^2)R^3}{\left|\mathrm{Y}_l^l\left(\frac{\pi}{2}, \xi\right)\right|^2 D_\alpha} \frac{\Delta\lambda_{min}}{\lambda} \qquad \textbf{Eq. 40}$$

where,

$$g(z) = \frac{6}{(2z)^2}(1 + e^{-2z}) - \frac{12}{(2z)^3}(1 - e^{-2z}), where\ z = \frac{a}{L_E} \qquad \textbf{Eq. 41}$$

and,

$$D_\alpha = \frac{4\pi n_e^2\left(n_p^2 - n_e^2\right)}{\left(n_p^2 + 2n_e^2\right)} \qquad \textbf{Eq. 42}$$

Assuming the particle lands exactly at the equator and that the smallest shift possible to see is $\Delta\lambda_{min}$ = 5 fm (which is quite small but has been achieved before[39]) we are able to numerically solve for the radius of the correspondingly smallest polystyrene particle (n_p = 1.57) with a BT resonator (n_s = 1.95) with radius R = 10,000 nm immersed in DI water (n_e = 1.326) excited by TE polarized light at wavelength, λ = 1063 nm we are able to plug in our above constants and calculated evanescent length to get a radius of, $a \approx 17$ nm.

VI. CONCLUSION

Unfortunately this is not enough to be able to detect an RNAP enzyme. According to Finn *et al.*[50] the structure of the core *Escherichia coli* RNAP (of sub-unit make-up α, α, β, β' and ω) has an asymmetric shape with lengths along its body of up to 15 nm. Using this as a rough gauge of the diameter of a spherical object the target sensitivity required would be 7.5 nm.

The new sensitivity required can be estimated. Now suppose we take a ratio of equation 21 for two different particle sizes landing on the same resonator, we get:

$$\frac{{a_1}^3 g(z_1)}{{a_2}^3 g(z_2)} \approx \frac{\Delta\lambda_{min1}}{\Delta\lambda_{min2}} \qquad \textbf{Eq. 43}$$

with a_1 being the previous calculation of ~17 nm, a_2 the target radius of 7.5 nm and z_1 and z_2 their respective radii divided by evanescent field. , $\Delta\lambda_{min1}$ = 5 fm and so the resultant minimum detectable shift should be, $\Delta\lambda_{min2}$ = 0.48 fm. A number which is unrealistic to achieve for the system detailed here.

Fortunately there are ways to get around this, for example, it is possible to decrease the radius. We can use a similar technique to evaluate the new radius:

$$\frac{{a_1}^3 g(z_1)}{{a_2}^3 g(z_2)} \approx \frac{{R_1}^3}{{R_2}^3} \qquad \textbf{Eq. 44}$$

Although not totally accurate we will assume that the evanescent field length remains constant. R_2 = 4,600 nm. Similarly, if Q degradation due to increasing curvatures become

a problem then another option to consider in tandem is to use another material with higher refractive index. Literature has already cited the use of TiO_2 for WGM purposes due to having high indices of refraction (generally over 2 around a wavelength of light near 1 micron).

Furthermore, a different wavelength laser can be used, one that lases at lower wavelengths which would serve to lessen Q degradation via water absorption. And lastly, as has been seen using LFA, particles can be pulled to the surface within a 650 nm arc distance which could be useful in arranging plasmonic particles upon the surface of the microsphere in a way that might facilitate bio-complex sensing. As has been demonstrated in the past, plasmonics in conjunction with silica resonators has been able to see down to ~5kDa whereas RNAP is ~400kDa, providing sufficient sensitivity for the task. However, plasmonics can also be combined with higher refractive index materials for even larger gains in sensitivity.

Thus, in conclusion, this thesis has shown proof of principle that smaller radius resonators with higher refractive indices are able to resonate and retain high Q values which facilitates sensing. Additionally, a preliminary proof of principle has been shown for LFA, which can also serve the purpose of bio-complex sensing. Going forward, there are a plethora of options open to try and it will be the goal of my Ph.D. work to build a size/mass spectrometer for bio-complex sensing.

VII. WORKS CITED

[1] Bar-Nahum G, Epshtein V, Ruckenstein AE, Rafikov R, Mustaev A, Nudler E A ratchet mechanism of transcription elongation and its control. Cell. 28 Jan 2005. 120(2):183-93

[2] Bratton BP, Mooney RA, Weisshaar JC. Spatial Distribution and Diffusive Motion of RNA Polymerase in Live Escherichia coli. Journal of Bacteriology. 2011;193(19):5138-5146. doi:10.1128/JB.00198-11.

[3] Dulin, D., Lipfert, J., Moolman, M.C. and Dekker, N.H. (2013) Studying genomic processes at the single-molecule level: introducing the tools and applications. Nature Reviews Genetics, 14, 9-22.

[4] Grohmann, D., Werner, F. and Tinnefeld, P. (2013) Making connections - strategies for single molecule fluorescence biophysics. Current Opinion in Chemical Biology, 17, 691- 698

[5] Joo, C., Fareh, M. and Kim, V.N. (2013) Bringing single-molecule spectroscopy to macromolecular protein complexes. Trends in Biochemical Sciences, 38, 30-37.

[6] Finkelstein, I.J. and Greene, E.C. (2008) Single molecule studies of homologous recombination. Mol. Biosyst., 4, 1094-1104.

[7] Lodish H, Berk A, Zipursky SL, et al. Molecular Cell Biology. 4th edition. New York: W. H. Freeman; 2000. Section 10.6, RNA Polymerase II Transcription-Initiation Complex.

[8] Vollmer, F., Arnold, S., Keng, D., (2008) Single Virus Detection From the Reactive Shift of a Whispering-Gallery Mode. PNAS, vol 105, no 52, 20701-20704

[9] Schramm, L., Nouria, H., Recruitment of RNA polymerase III to its target promoters. Genes & Dev. 2002. 16:2593-2620

[10] Henri C. Buc, Terence Strick, RNA Polymerases as Molecular Motors. Volume 16 of RSC Biomolecular Sciences, Royal Society of Chemistry, 2009, 220-229

[11]Evgeny Nudler, RNA Polymerase Backtracking in Gene Regulation and Genome Instability, Cell, Volume 149, Issue 7, 22 June 2012, Pages 1438-1445, ISSN 0092-8674, http://dx.doi.org/10.1016/j.cell.2012.06.003.

[12] Paule, M. R., & White, R. J. (2000). Transcription by RNA polymerases I and III. *Nucleic Acids Research*, *28*(6), 1283–1298.

[13] Selvin, P.R. (2000) The renaissance of fluorescence resonance energy transfer. *Nat. Struct. Biol.*, **7**, 730-734.

[14] Axelrod, D. (2001) Total internal reflection fluorescence microscopy in cell biology. *Traffic*, **2**, 764-774.

[15] Levene, M.J., Korlach, J., Turner, S.W., Foquet, M., Craighead, H.G. and Webb, W.W. (2003) Zero-mode waveguides for single-molecule analysis at high concentrations. *Science*, **299**, 682-686.

[16] Axelrod, D; Koppel, D; Schlessinger, J; Elson, E; Webb, W (1976). "Mobility measurement by analysis of fluorescence photobleaching recovery kinetics". Biophysical Journal 16 (9): 1055–69.

[17] Hell, Stefan W., and Jan Wichmann. "Breaking the diffraction resolution limit by stimulated emission: stimulated-emission-depletion fluorescence microscopy." Optics letters 19.11 (1994): 780-782.

[18] "A single molecule immunoassay by localized surface plasmon resonance" Kathryn M Mayer et al 2010 Nanotechnology 21 255503

[19] Ament, I., Prasad, J., Henkel, A., Schmachtel, S. and Sonnichsen, C. (2012) Single unlabeled protein detection on individual plasmonic nanoparticles. Nano Lett., 12, 1092- 1095.

[20] Zijlstra, P., Paulo, P.M.R. and Orrit, M. (2012) Optical detection of single non-absorbing molecules using the surface plasmon resonance of a gold nanorod. Nat. Nanotechnol., 7, 379-382.

[21] Label-Free Detection of Single Protein Using a Nanoplasmonic-Photonic Hybrid Microcavity Venkata R. Dantham, Stephen Holler, Curtis Barbre, David Keng, Vasily Kolchenko, and Stephen Arnold Nano Letters 2013 13 (7), 3347-3351 DOI: 10.1021/nl401633y

[22] Keng, D., Tan, X., Arnold, S., (2014) Whispering Gallery Micro-global Position System for Nanoparticle Sizing in Real Time. App. Phys. Let., 105, 071105

[23] http://www.stpauls.co.uk/Cathedral-History/Explore-the-Cathedral/Climb-the-Dome

[24] Lord Rayleigh, Theory of Sound, vol. II, 1st edition, (London, MacMillan), 1878.

[25] "Whispering-Gallery Phenomena at St. Paul's Cathedral." [Online]. Available: http://www.nature.com/nature/journal/v108/n2706/abs/108042a0.html. [Accessed: 11-Jun-2015].

[26] Arnold, S., Khoshsima, M., Teraoka, I., Holler, S., & Vollmer, F. (2003). Shift of whispering-gallery modes in microspheres by protein adsorption. *Optics Letters*, *28*(4), 272–274. http://doi.org/10.1364/OL.28.000272

[27] Hill, S.C., Brenner, R.E. "Morphology-Dependent Resonances" in *Optical Effects Associated with Small Particles*, Ed. By P.W. Barber and R.K. Chang, World Scientific, Singapore (1988).

[28] Little, B. E., Laine, J. P., & Haus, H. a. (1999). Analytic theory of coupling from tapered fibers and half-blocks into microsphere resonators. *Journal of Lightwave Technology*, *17*(4), 704–715. http://doi.org/10.1109/50.754802

[29] Arnold, S., Holler, S. "Microparticle Photophysics: Fluorescence Microscopy and Spectroscopy of a Photonic Atom" in Cavity Enhanced Spectroscopies, Eds.R.D.Van Zee and J.P.Looney, pp.227-253, Aademic Press (2002).

[30] Vollmer, F. (2004). *Resonant Detection of Nano to Microscopic Objects Using Whispering Gallery Modes*. *Thesis*. The Rockefeller University.

[31] Vollmer, F., & Arnold, S. (2008). Whispering-gallery-mode biosensing: label-free detection down to single molecules. *Nature Methods*, *5*(7), 591–596. http://doi.org/10.1038/nmeth.1221

[32] S. Arnold, M. Khoshsima, I. Teraoka, S. Holler, and F. Vollmer, "Shift of whispering-gallery modes in microspheres by protein adsorption," Opt. Lett. 28, 272-274 (2003)

[33] Lam, C. C., Leung, P. T., & Young, K. (1992). Explicit asymptotic formulas for the positions, widths, and strengths of resonances in Mie scattering. *Journal of the Optical Society of America B*, *9*(9), 1585. http://doi.org/10.1364/JOSAB.9.001585

[34] Swindal, J. C., Leach, D. H., Chang, R. K., & Young, K. (1993). Procession of morphology-dependent resonances in nonspherical droplets. *Optics Letters*, *18*(3), 191. http://doi.org/10.1364/OL.18.000191

[35] Lai, H.M., Leung, P.T., Barber, P.W., Young, K., Hill, S. C. (1990). Time-independent perturbation for leaking electromagnetic modes in open systems with application to resonances in microdroplets. *Phys. Rev. A*, *41*(9).

[36] Jackson, J.D. (1975) *Classical Electrodynamics*. 2nd ed. John Wiley & Sons, New York.

[37] Arnold, S., Ramjit, R., Keng, D., Kolchenko, V. and Teraoka, I. (2008) MicroParticle photophysics illuminates viral bio-sensing. *Faraday Discuss.*, **137**, 65-83.

[38] Keng, D., Tan, X., & Arnold, S. (2014). Whispering gallery micro-global positioning system for nanoparticle sizing in real time. *Applied Physics Letters*, *105*(7), 071105. http://doi.org/10.1063/1.4893762

[39] Arnold, S., Keng, D., Shopova, S. I., Holler, S., Zurawsky, W., & Vollmer, F. (2009). Whispering Gallery Mode Carousel--a photonic mechanism for enhanced nanoparticle detection in biosensing. *Optics Express*, *17*(8), 6230–6238. http://doi.org/10.1364/OE.17.006230

[40] Dill, Ken A. and Bromberg, S. (2003). Salt Ions Shield Charged Objects in Solution. In *Molecular Driving Forces: Statistical Thermodynamics in Chemistry and Biology* (2nd ed., pp. 433–447). Garland Science, 2003.

[41] www.fiber-optic-cables-plus.com

[42] http://web.arizona.edu/~lascool/research/spin.html

[43] Arnold, S., Ramjit, R., Keng, D., Kolchenko, V., & Teraoka, I. (2008). MicroParticle photophysics illuminates viral bio-sensing. *Faraday Discussions*, *137*, 65–83; discussion 99–113. http://doi.org/10.1039/b702920a

[44] Mikhail L. Gorodetsky, A. A. S. and V. S. lichenko. (1996). On the ultimate Q of optical microsphere resonators. *Optics Letters*, *2799*, 389–391.

[45] Vladimir S. Ilchenko ; X. S. Yao ; Lute Maleki; High-Q microsphere cavity for laser stabilization and optoelectronic microwave oscillator. Proc. SPIE 3611, Laser Resonators II, 190 (May 24, 1999); doi:10.1117/12.349244.

[46] Chen, Y. (2012). *Polymer Microsphere Attachment to a Silicon Telecom Fiber for Whispering Gallery Mode Biosensing*.

[47] Israelachvili, J. N. (2010). *Intermolecular and Surface Forces* (3, illustr). Academic Press. Retrieved from https://books.google.com/books/about/Intermolecular_and_Surface_Forces.html?id=MVbWBhubrgIC&pgis=1

[48] Svitelskiy, O., Li, Y., Darafsheh, A., Sumetsky, M., Carnegie, D., Rafailov, E., & Astratov, V. N. (2011). Fiber coupling to BaTiO3 glass microspheres in an aqueous environment. *Optics Letters*, *36*(15), 2862–2864. http://doi.org/10.1364/OL.36.002862

[49] Thorne, A., Litzén, U., & Johansson, S. (1999). *Spectrophysics: Principles and Applications*. Springer Science & Business Media. Retrieved from https://books.google.com/books?id=SF8fdwacahkC&pgis=1

[50] Finn, R. D., Orlova, E. V., Gowen, B., Buck, M., & Van Heel, M. (2000). Escherichia coli RNA polymerase core and holoenzyme structures. *EMBO Journal*, *19*(24), 6833–6844. http://doi.org/10.1093/emboj/19.24.6833